JOURNAL OF GEOPHYSICAL RESEARCH, VOL. 101, NO. A12, PAGES 26,697–26,718, DECEMBER 1, 1996

High-latitude ionospheric electrodynamics as determined by the assimilative mapping of ionospheric electrodynamics procedure for the conjunctive SUNDIAL/ATLAS 1/ GEM period of March 28-29, 1992

G. Lu,[1] B. A. Emery,[1] A. S. Rodger,[2] M. Lester,[3] J. R. Taylor,[3] D. S. Evans,[4] J. M. Ruohoniemi,[5] W. F. Denig,[6] O. de la Beaujardière,[7] R. A. Frahm,[8] J. D. Winningham,[8] D. L. Chenette[9]

Abstract. During the conjunctive SUNDIAL/ATLAS 1/GEM campaign period of March 28–29, 1992, a set of comprehensive data has been collected both from space and from ground. The assimilative mapping of ionospheric electrodynamics (AMIE) procedure is used to derive the large-scale high-latitude ionospheric conductivity, convection, and other related quantities, by combining the various data sets. The period was characterized by several moderate substorm activities. Variations of different ionospheric electrodynamic fields are examined for one substorm interval. The cross-polar-cap potential drop, Joule heating, and field-aligned current are all enhanced during the expansion phase of substorms. The most dramatic changes of these fields are found to be associated with the development of the substorm electrojet in the post midnight region. Variations of global electrodynamic quantities for this 2-day period have revealed a good correlation with the auroral electrojet (AE) index. In this study we have calculated the *AE* index from ground magnetic perturbations observed by 63 stations located between 55° and 76° magnetic latitudes north and south, which is larger than the standard *AE* index by about 28% on the average over these 2 days. Different energy dissipation channels have also been estimated. On the average over the 2 days, the total globally integrated Joule heating rate is about 102 GW and the total globally integrated auroral energy precipitation rate is about 52 GW. Using an empirical formula, the ring current energy injection rate is estimated to be 125 GW for a decay time of 3.5 hours, and 85 GW for a decay time of 20 hours. We also find an energy-coupling efficiency of 3% between the solar wind and the magnetosphere for a southward interplanetary magnetic field (IMF) condition.

[1]High Altitude Observatory, National Center for Atmospheric Research, Boulder, Colorado.

[2]British Antarctic Survey, Cambridge, England.

[3]Department of Physics and Astronomy, University of Leicester, Leicester, England.

[4]Space Environment Laboratory, National Oceanic and Atmospheric Administration, Boulder, Colorado.

[5]Applied Physics Laboratory, Johns Hopkins University, Laurel, Maryland.

[6]Phillips Laboratory, Hanscom Air Force Base, Massachusetts.

[7]National Science Foundation, Arlington, Virginia.

[8]Southwest Research Institute, San Antonio, Texas.

[9]Lockheed Palo Alto Research Laboratory, Palo Alto, California.

Paper number 96JA00513.
0148-0227/96/96JA-00513$05.00

1. Introduction

High-latitude ionospheric convection, auroral precipitation, and electric currents are the manifestations of solar wind and magnetospheric energy coupling into the ionospheric-thermospheric system. Therefore the high-latitude ionosphere provides an important linkage between the solar wind-magnetosphere environment and the dynamics of the Earth's upper atmosphere [e.g., *Killeen et al.*, 1984; *Forbes and Harel*, 1989; *Crowley et al.*, 1989; *Thayer and Vickrey*, 1992; *Deng et al.*, 1993; *Lu et al.*, 1995]. Understanding how energy is transmitted from the magnetosphere through ionosphere to the thermosphere is one of the most important tasks of geophysics.

In a continuing effort to quantitatively understand and accurately model these coupling mechanisms and their manifestations in the ionospheric-thermospheric

system, the first Atmospheric Laboratory for Applications and Science (ATLAS 1) mission was flown on the *Atlantis* space shuttle from March 24 to April 2, 1992. The mission focused on the chemistry, energetics, and electrodynamics of the ionospheric-thermospheric system through the comprehensive nature of its own measurements combined with around-the-clock global observations of the SUNDIAL network of ionosondes and radars (*Szuszczewicz et al.* [this issue]). In conjunction with the SUNDIAL/ATLAS 1 mission, a Geospace Environment Modeling (GEM) campaign was taking place on March 28 and 29. The GEM campaigns are coordinated multi-instrument observations with the aim of understanding magnetospheric processes and their coupling with the solar wind and the ionosphere. A variety of data collected during the campaign is combined to construct large-scale instantaneous patterns of the high-latitude ionospheric conductivity, convection, and other related quantities, using the assimilative mapping of ionospheric electrodynamics (AMIE) procedure [*Richmond and Kamide*, 1988; *Richmond*, 1992]. The purpose of this paper is to examine the high-latitude ionospheric electrodynamic activity for this 2-day period.

Distributions of the ionospheric convection and auroral precipitation are also important inputs to simulation models of ionospheric and thermospheric dynamics, such as the National Center for Atmospheric Research Thermosphere-Ionosphere General Circulation Model (NCAR-TIGCM) [*Roble et al.*, 1988]. In companion papers, *Szuszczewicz et al.* [this issue] and *Emery et al.* [this issue] compare the F region measurements from a global network of ionosonde stations taken during the ATLAS 1 mission with the model predictions from TIGCM. Using realistic ionospheric inputs to the thermospheric simulation models allows meaningful comparison between observations and model predictions, especially during coordinated campaign studies.

In a previous study [*Lu et al.*, 1995], we have used realistic time-dependent high-latitude ionospheric convection and auroral precipitation patterns derived from AMIE as inputs to the TIGCM to investigate how the magnetospheric energy inputs affect the thermospheric dynamics as well as the feedback of the thermospheric neutral wind dynamo onto magnetospheric electrodynamics. The focus of that study was mainly on the TIGCM results. In this paper we present and discuss the AMIE results. Additional data sets have been added to improve the estimates of the high-latitude ionospheric electrodynamic fields since the previous study. A detailed description of all data that are incorporated into AMIE is given in the next section.

2. Data and Procedure

2.1. Data Inputs

Satellite observations. During this 2-day period, several satellites provided data to the assimilation of global electrodynamic fields. The IMP 8 satellite was located upstream of the Earth at about (31,-16,-16) R_E in GSE coordinates at 1500 UT on March 29, 1992. Unfortunately, the interplanetary magnetic field (IMF) and solar wind plasma data were only measured for about 6 hours during the 2 days under study. Plotted in Figure 1 is the IMP 8 data taken between 1320 and 1930 UT on March 29. The top three panels show the x, y, and z components (in GSM coordinates) of the IMF. During the interval, B_x oscillated in sign frequently and B_y and B_z were negative for most of the interval, but the magnitudes of both components varied between about 0 nT and -6 nT. Except for a few spikes due to instrumental noise, the solar wind speed and density shown in the bottom two panels were almost steady, around 350 km/s and 12 cm^{-3}, respectively.

During the period of March 28–29, 1992, there were four Defense Meteorological Satellite Program (DMSP) spacecraft F8-F11 operating in Sun-synchronous polar circular orbits at altitudes of about 840 km, with orbital inclinations of 98.7° and orbital periods of 100 min. All four DMSP satellites measured the cross-track horizontal and vertical ion drift components, with F10 and F11 also measuring the along-track component. Because of some technical difficulties in reducing the along-track component, only the cross-track ion drifts or the along-track electric fields were incorporated into AMIE. The electric fields were mapped along the magnetic field lines to a reference altitude of 110 km and averaged to a 20-s time resolution before being fed into AMIE. The DMSP satellites also provided measurements of auroral precipitating particles within the 32 eV to 30 keV energy range. Since only high-energy particles penetrate into the lower thermosphere where the conductivity peaks, only those precipitating electrons with energies between 460 eV and 30 keV [*Rich et al.*, 1987] were considered in estimating the Pedersen and Hall conductances. The DMSP particle data were averaged in 30-s segments.

NOAA 12 is also a polar-orbiting satellite which has an altitude of 850 km and an orbital period of 100 min. The primary data provided by the NOAA 12 satellite were the fluxes of energetic particles in the 300 eV to 20 keV energy range averaged over about 40-s intervals.

The Upper Atmospheric Research Satellite (UARS) is in a near-circular orbit at about 585 km, with an inclination of 57°. The Atmospheric X ray Imaging Spectrogram (AXIS) instrument of the Particle Environment Monitor (PEM) experiment on board UARS measures 3- to 100-keV X rays in 16 pixels covering 2000 km along the Earth's surface perpendicular to the satellite track every 8 s (for detailed instrumentation, see *Chenette et al.* [1993] and *Winningham et al.* [1993]). X rays are generated by the energetic electrons as they are precipitating into the atmosphere. The characteristic energy and energy flux of precipitating electrons are extracted from the X ray spectrum [*Chenette et al.*, 1993] and the results are binned over neighboring pixels and averaged to 1-min resolution.

The Japanese satellite Exos D is in an orbital inclination of 75° and orbital period 212 min. The apogee and perigee of the satellite are 10,500 km and 270 km, respectively. During the March 1992 period, the satel-

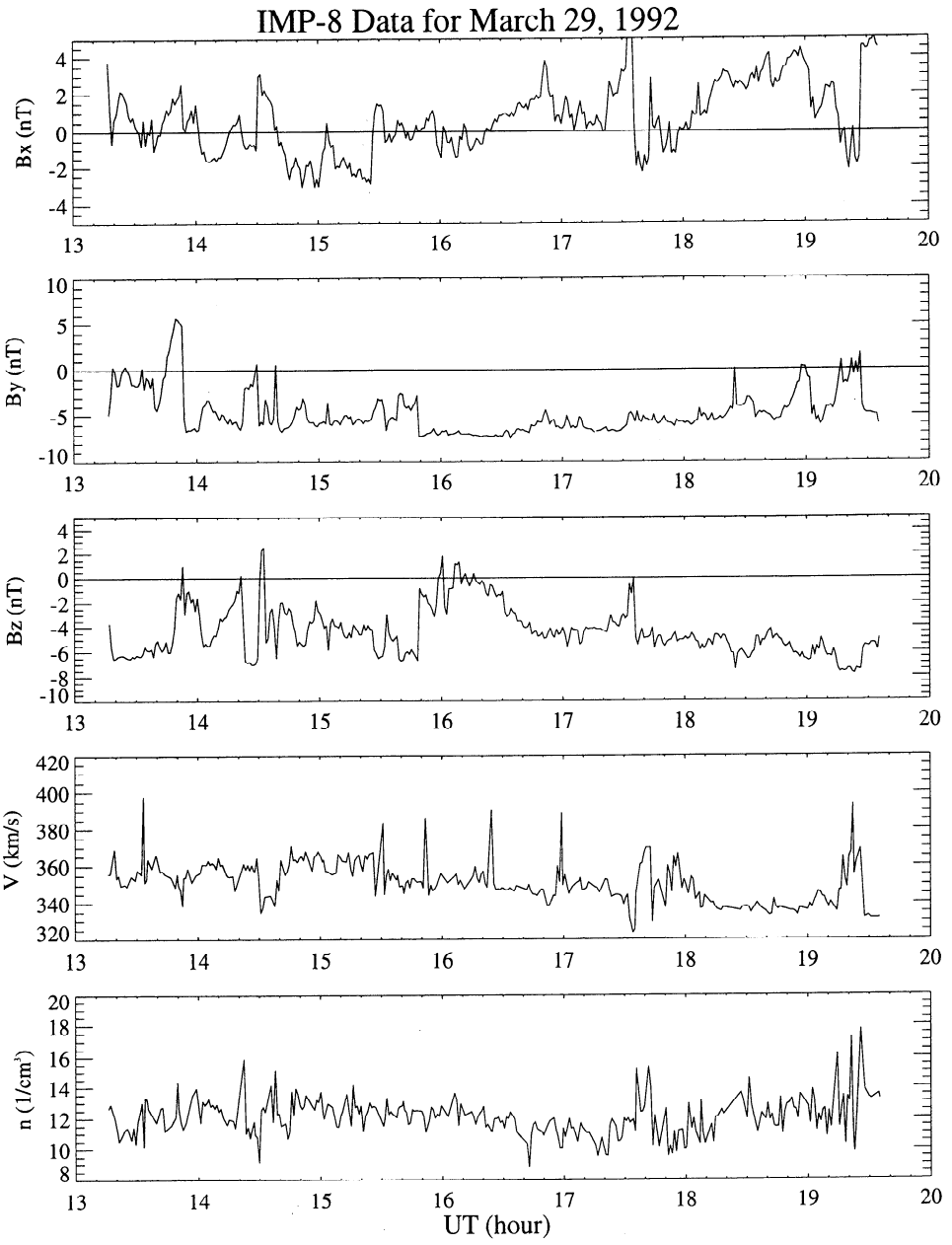

Figure 1. 1-min interplanetary magnetic fields (in GSM coordinates) and solar wind plasma measured by the IMP 8 satellite between 1300 UT and 2000 UT on March 29, 1992.

lite altitude varied from about 1100 km to 8500 km over the northern polar region. No data were obtained from the satellite when it was passing over the southern hemisphere because the ground receivers in the southern hemisphere were not operating during that period. Exos D measured the two components of the electric field perpendicular to the satellite spin axis, and the vector electric field was calculated with the assumption that the electric field is perpendicular to the main magnetic field (see *Hayakawa et al.* [1990] for further information). In addition, both UARS and Exos D provided measurements of magnetic perturbations [*Winningham et al.*, 1993; *Fukunishi et al.*, 1990] by subtracting the measured vector magnetic field from the International Geomagnetic Reference Field (IGRF) 1990 model of the Earth's main field. The data from UARS and Exos D instruments were incorporated into AMIE for the first time.

Radar measurements. The Sondrestrom incoherent scatter radar was operating between 0440 and 2000 UT on March 29, 1992. Vector ion drift velocities were extracted from the line-of-sight components and binned over 1° intervals between 72° and 76° magnetic latitude every 5 min. The Wick VHF coherent scatter radar, originally part of the Sweden and Britain Radar Experiment (SABRE), measured E region line-of-sight irregularity drifts from 0000 UT on March 28 until 0506

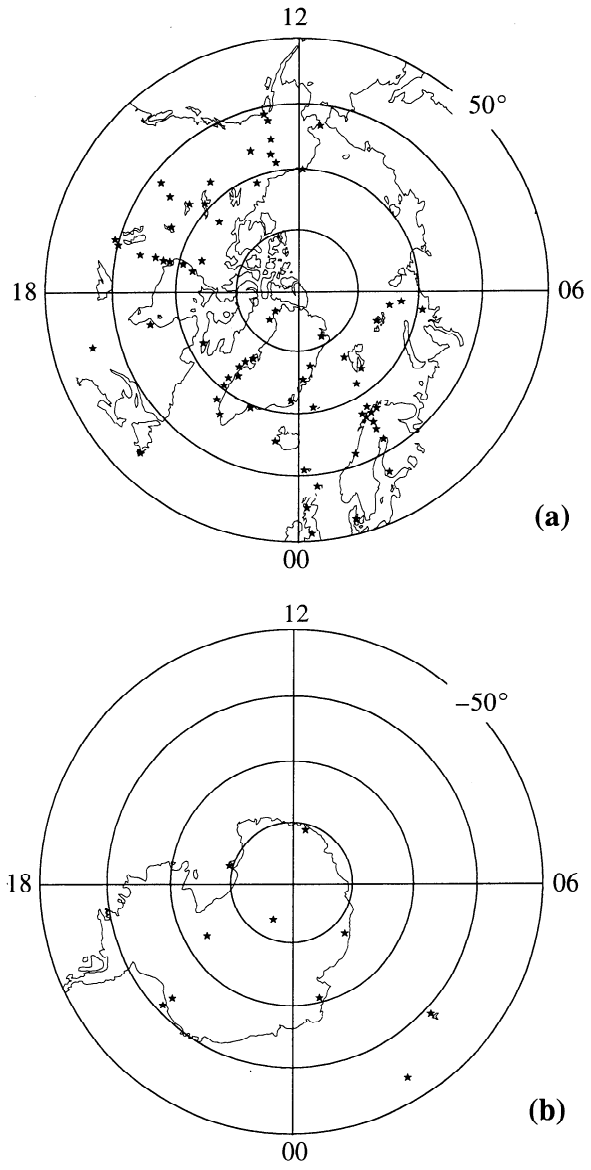

Figure 2. Map of ground magnetometer stations at 0000 UT in the (top) northern and (bottom) southern hemispheres in apex magnetic coordinates, with the magnetic pole at the center and magnetic local time shown around the periphery of the dial. Stations poleward of ±50° magnetic latitude are indicated by stars.

UT on March 29 with the data averaged every 5 min over 1° bins between 60° and 68° magnetic latitude. During this 2-day period, the Goose Bay HF coherent scatter radar provided vector ion drift velocities which were averaged every 10 min over 2° bins from 65° to 81° magnetic latitude. The Halley Bay HF coherent radar in Antarctica also provided vector velocities which were averaged each 10 min in 1° magnetic latitude bins ranging from -63° to -83°. The Goose Bay and Halley Bay radars are approximately magnetically conjugate.

Ground magnetometers. During this campaign period, the ground magnetic perturbations were measured by 93 magnetometer stations with 14 located in the southern hemisphere. Figure 2 shows the locations of the magnetometer stations poleward of 50° magnetic latitude in the northern and southern hemispheres as indicated by stars. All three components of the magnetometer data were used in the study. The magnetometer data were averaged to 5-min resolution. The effect of magnetospheric currents, such as the ring current and the magnetopause currents, is removed by subtracting $D_{st} \cos|\theta|$ from the north-south component of the magnetic perturbations (where θ is magnetic latitude).

The auroral electrojet (AE) index is the most commonly used indicator of substorm activity. The standard AE index (commonly referred to as $AE(12)$) is based on the ground magnetic perturbations in the north-south component from 12 selected auroral zone stations in the northern hemisphere. The standard AE index is an imperfect measure of electrojet strength. The fact that the auroral zone varies in latitude from time to time causes problems for this index, and the designated AE stations tend to miss the intense electrojet regions for very active or very quiet conditions. A large collection of ground magnetometer data during coordinated campaigns allows us to calculate the AE index from a number of stations. During the conjunctive SUNDIAL/ATLAS 1/GEM period of March 28–29, 1992, there were 63 ground stations located between 55° and 76° magnetic latitudes north and south. The AE index based on the measurements from these 63 stations (i.e., $AE(63)$) represents substorm activity more accurately. See section 3 for more details.

2.2. AMIE Procedure

The AMIE procedure is an optimally constrained, weighted least squares fit of coefficients to the observed data. The procedure first estimates the height-integrated Pedersen and Hall conductivities by modifying statistical models. In this study, statistical Pedersen and Hall conductivity models are obtained by combining the auroral conductivity model of *Fuller-Rowell and Evans* [1987] with the conductances produced by solar extreme ultraviolet (EUV) radiation. The auroral conductivity model is parameterized by the 10-level Hemispheric Power Index (HPI) [*Foster et al.*, 1986]. Energy fluxes and average energies of the auroral precipitating electrons measured by the DMSP and UARS satellites are used to calculate the height-integrated Pedersen and Hall conductivities, based on the empirical formulas of *Robinson et al.* [1987]. The estimates of the conductivities from the NOAA 12 data are based on an electron transport code under the full energy spectrum of the electron precipitation [*Fuller-Rowell and Evans*, 1987]. In addition, the magnetic perturbations as measured by ground-based magnetometers are used to modify the ionospheric conductivities [*Ahn et al.*, 1983b] and provide an improved temporal and spatial resolution of high-latitude ionospheric conductances. The detailed fitting procedure has been described by *Richmond and Kamide* [1988] and *Richmond et al.* [1988]. We incorporate simultaneous observations from both hemispheres, assuming that the auroral precipitation is approximately conjugate. But observations from the op-

posite hemisphere are weighted 50% less in the fitting.

Ionospheric electric fields and currents are related by Ohm's law, through the Pedersen and Hall conductivities. Thus, once a reliable conductivity distribution is derived, the ionospheric convection pattern can be estimated from the direct ion drift observations by satellites and radars, and from the inversion of magnetic perturbations. Additionally, an a priori statistical potential model is often applied, which provides a first-order estimate of the ionospheric potentials where there are no in situ measurements. The statistical electric potential model used in this study is based on Millstone Hill radar observations [*Foster et al.*, 1986], and is also parameterized by the HPI index. The different data sets are weighted by the inverse square of their effective errors so that less reliable data contribute less to the fitting. AMIE uses apex coordinates [*VanZandt et al.*, 1972; *Richmond*, 1995] with the apex latitude being similar to invariant latitude and corrected geomagnetic latitude in polar regions. All data are converted to apex coordinates before being incorporated into AMIE. The current grid size of AMIE is about 1.7° in latitude and 10° in longitude.

3. Results

3.1. Examination of Large-Scale Electrodynamic Patterns

The period of March 28–29, 1992, is featured by a series of moderate substorms. In this subsection we examine the large-scale patterns of ionospheric convection, Joule heating, and field-aligned current density during a substorm interval between 0800 and 1200 UT on March 29. This is the third largest substorm during this 2-day period in terms of the magnitude of the AE index; the other two largest substorms are associated with either an ambiguous onset time (AE peaks at about 0510 UT on March 29) or a poor coverage of ground magnetometers over the Russian area near local midnight (AE peaks at 1550 UT on March 29). According to the distribution of the AL and AE indices (see Figure 7a and the text in the next section), the substorm starts at about 0810 UT when the magnitudes of AL and AE start to increase abruptly. The substorm expansion phase exhibits an oscillatory nature and lasts until about 1015 UT. After that, the substorm is in the recovery phase as AL and AE gradually diminish, until about 1200 UT. Ionospheric electrodynamic fields at six selected UT times within the substorm are examined in detail (described below in the text) and results are shown in Figures 3–6. The times of interest are 0810 UT when the onset of the expansion phase occurs; 0840 UT and 0910 UT in the expansion phase; 0940 UT and 1000 UT as peaks of the expansion phase when the derived AE index reaches maxima; and 1030 UT in the recovery phase. It is worth pointing out that this is not a case of a clear and isolated substorm event. This interval is more likely a superposition of two or more smaller substorms, which can be seen as AL and AE increase nonmonotonically during the expansion phase. Therefore, identification of various substorm phases based on the AL and AE indices is rather crude. Nevertheless, our intention is to demonstrate the variations of the different electrodynamic parameters associated with geomagnetic activity.

The high-latitude electrodynamic fields shown in Figures 3–6 are derived from data sources described in the previous section. Satellite precipitating particle observations and radar ion drift measurements taken within ±5 min of each analyzed time are utilized in the AMIE fitting procedure. The ground magnetometer data are averaged over 5-min in the vicinity of each given time. As we will discuss in the next section, the satellite ion drift or electric field measurements can have a significant influence on the cross-polar-cap potential drop. Therefore, in order to make a direct comparison between the patterns derived at different UT times during the substorm, we do not use the satellite ion drift data that are only available during a satellite overflight. However, we do utilize the satellite particle precipitation measurements to modify the ionospheric conductivities so that the inference of electric fields from the magnetometer data becomes more reliable.

Ionospheric convection. Figure 3 shows consecutive patterns of ionospheric convection during the substorm. The convection or electric potential contours are in solid lines where the AMIE procedure infers an uncertainty of less than 50% in the large-scale electric field; otherwise the contours are in dashed lines. The total cross-polar-cap potential drop given at the upper right corner of each pattern is the difference between the most positive and most negative potentials. At 0810 UT, the onset of the expansion phase, the convection pattern consists of two cells that are nearly symmetric about the noon-midnight meridian, but the positive potential dawn cell penetrates slightly into the pre-midnight region. The primary positive potential peak of the dawn cell is located at about 0200 magnetic local time (MLT) as indicated by the plus sign; in addition, there is a secondary positive potential peak at about 0630 MLT, which is not clearly visible with the 5-kV contour interval. At 0840 UT, the substorm expansion phase, the magnetic perturbations in the midnight and early morning sectors have increased dramatically. The enhanced magnetic perturbations also enhance the plasma convection, and the total cross-polar-cap potential drop rises from 42 kV to 65 kV. The double peaks on the dawnside are now both visible. The primary potential peak has moved to 0300 MLT while the secondary peak remains at the same location. The pattern at 0910 UT is nearly the same as that at 0840 UT, but the total potential drop is slightly smaller (61 kV). As mentioned above, this is not a typically isolated substorm event. A dip in the AL and AE indices is seen at about 0900 UT. At 0940 UT, the first peak of the expansion phase, the ground magnetic perturbations are most enhanced, and the cross-polar-cap potential drop reaches 78 kV. The nightside tip of the dawn cell has protruded into the pre-midnight region up to 2200 MLT. The primary potential

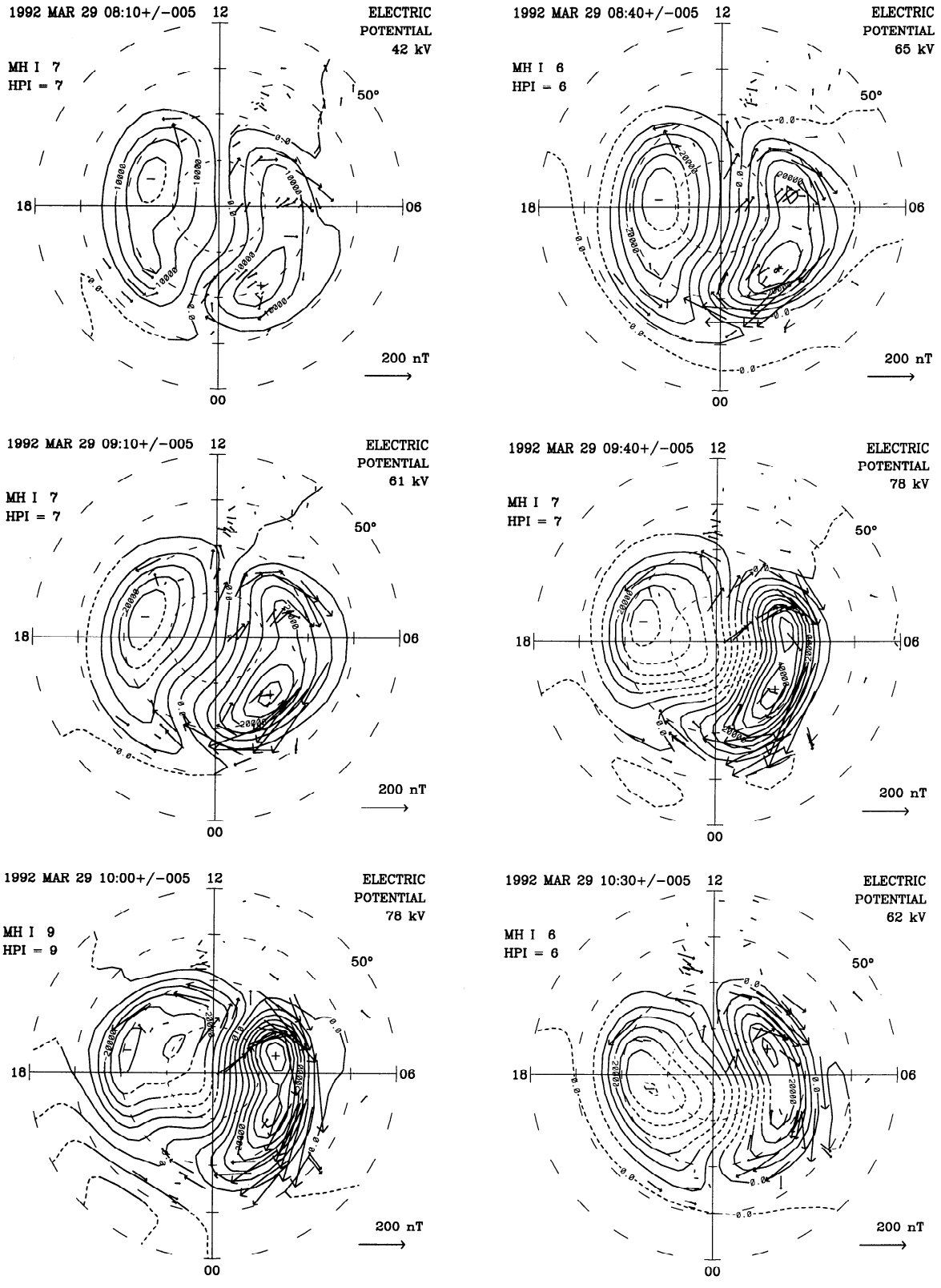

Figure 3. Consecutive northern hemispheric convection patterns derived between 0810 UT and 1030 UT. The patterns have a contour interval of 5 kV. The cross-polar-cap potential drop given at the upper right of each pattern is defined as the difference between the most positive and negative potential. Overlain are the horizontal magnetic perturbations which have been rotated 90° clockwise to indicate the direction of overhead equivalent current.

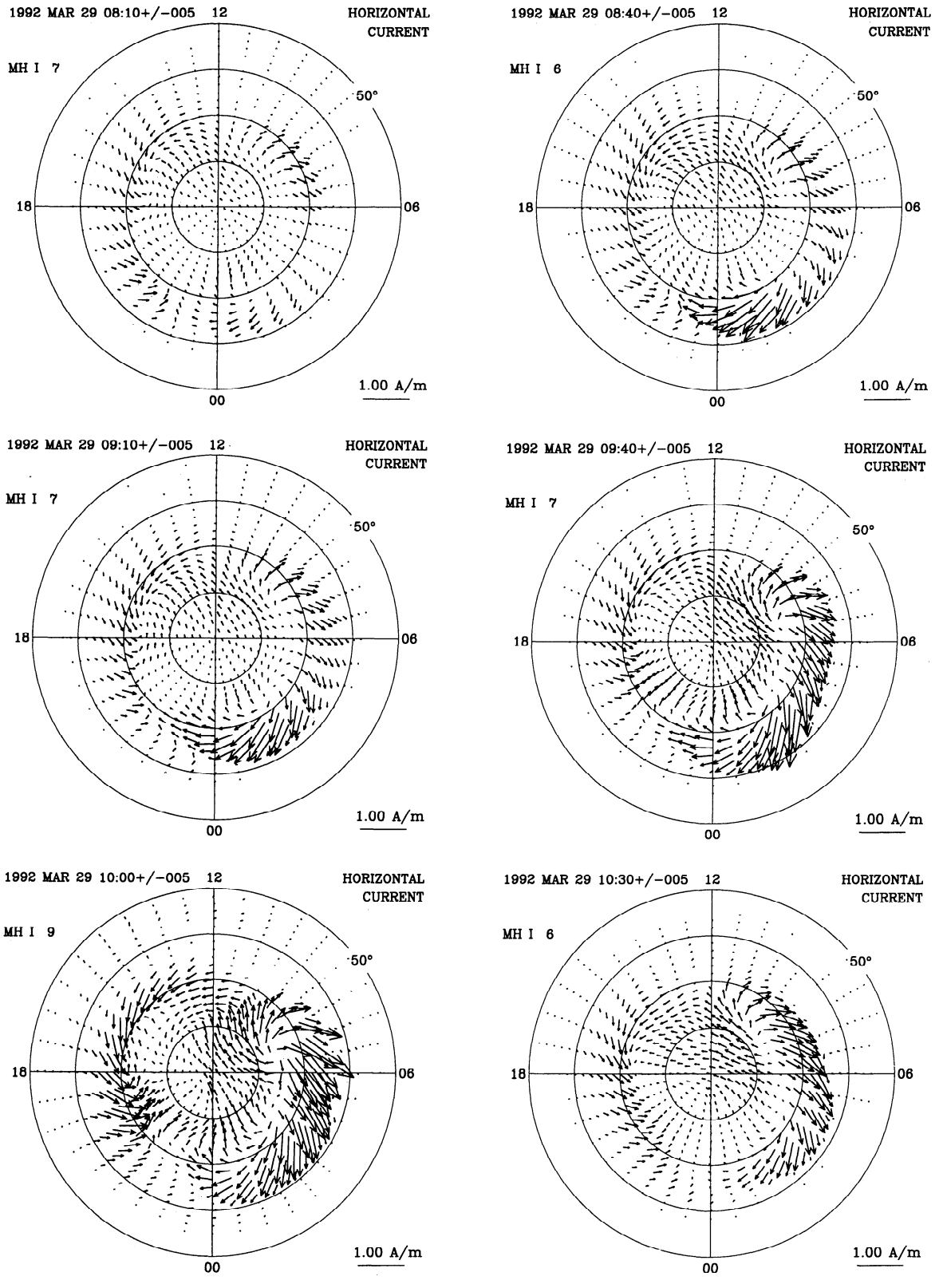

Figure 4. Patterns of ionospheric horizontal currents for the same time interval as Figure 3.

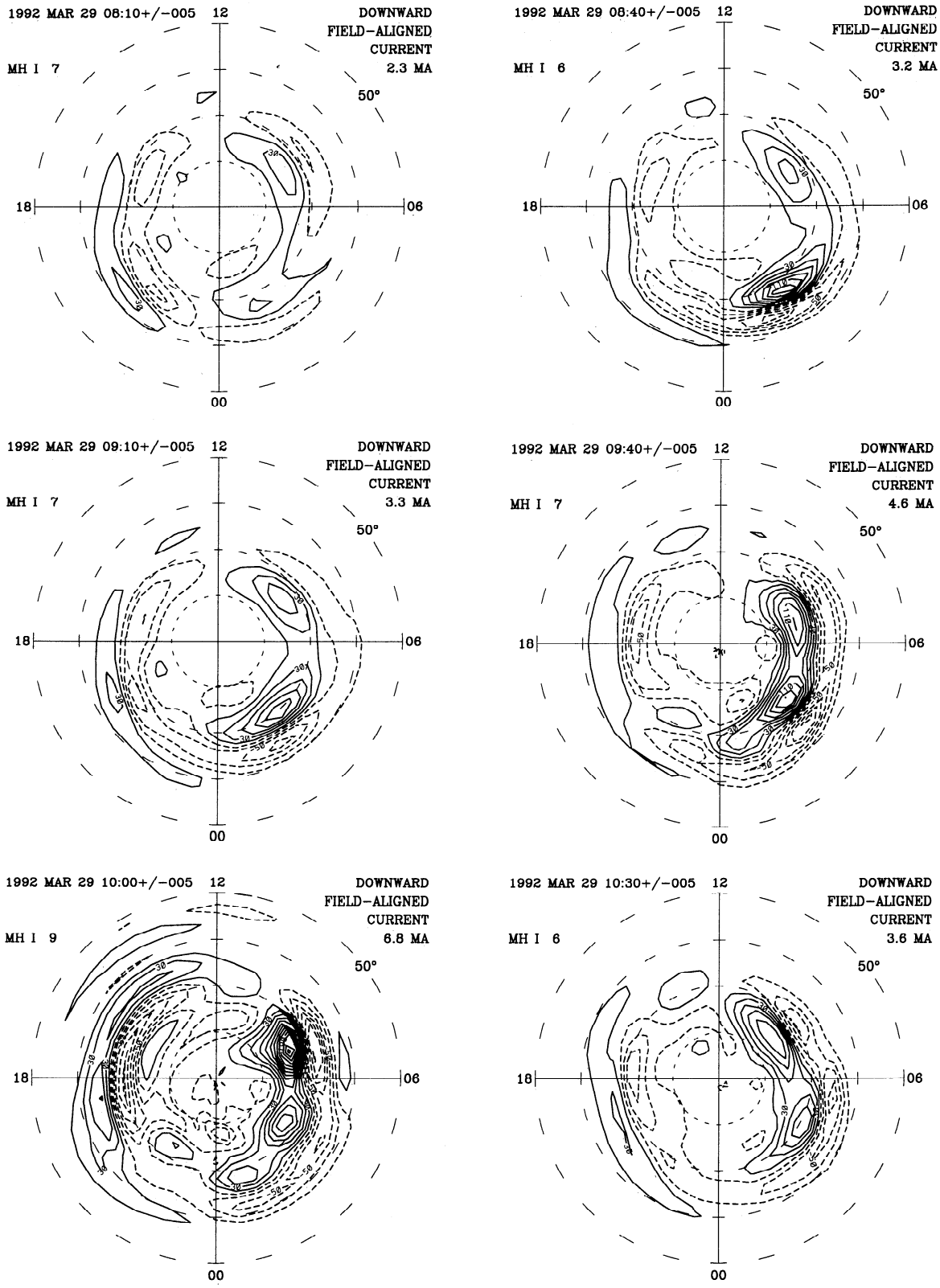

Figure 5. Distribution of field-aligned current for the same selected times as Figure 3. The contour interval is 0.2 $\mu A/m^2$, starting at ± 0.1 $\mu A/m^2$. Solid contours represent downward current and dashed contours upward current. The total downward current integrated poleward of 50° is given at the upper right of each pattern.

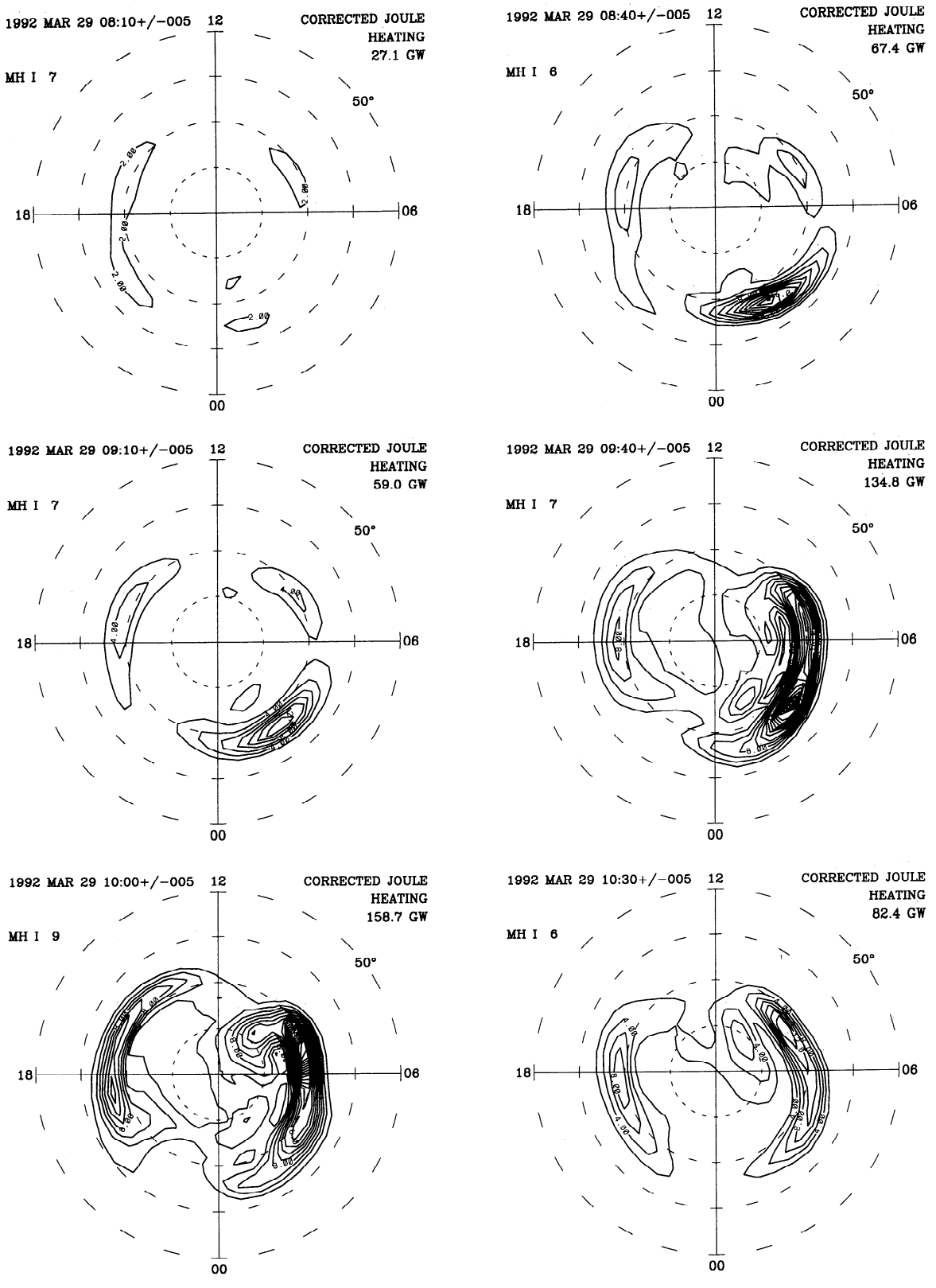

Figure 6. Distribution of height-integrated Joule heating during the same substorm period as Figure 3 with a contour interval of 2 mW/m^2. The total Joule heating integrated poleward of 50° is given in the upper right of each pattern.

peak now is located at 0400 MLT, and the secondary peak near dawn remains at the same location at about 0630 MLT. At 1000 UT, the second peak of the expansion phase, the magnetic perturbations are slightly weaker than at the previous peak in the midnight-to-early morning sector, but stronger near the dawn. At this time, the potential peak at 0630 MLT becomes the primary one, and the peak near 0400 MLT becomes secondary. At 1030 UT, the substorm recovery phase, the magnetic perturbations decrease further, and so does the cross-polar-cap potential drop. The potential peak in the morning sector becomes invisible as the substorm subsides.

As illustrated in Figure 3, a distinctive feature of the ionospheric convection or electric potential during the substorm is the formation of double potential peaks within the dawnside positive potential cell. As the substorm progresses, the potential peak in the post-midnight sector moves counterclockwise; whereas the peak near dawn remains nearly steady. A similar phenomenon was found by *Shue and Weimer* [1994] in their statistical study. As explained by *Kamide et al.* [1994], the peak near dawn represents the "normal" magnetospheric convection which is controlled mainly by the interaction between the solar wind and the magnetosphere, while the peak in the post-midnight sector is primarily caused by substorm activity, and therefore its motion directly reflects systematic variations associated with substorms.

Horizontal current. Variations of the horizontal ionospheric currents are shown in Figure 4. At the onset of the substorm expansion phase (0810 UT), there are three distinct current jets or electrojets: (1) the eastward electrojet between 1200 and 2200 MLT; (2) the westward electrojet between 0600 and 1100 MLT; and (3) the westward electrojet between 2300 and 0300 MLT. These currents are primarily Hall currents. Spatial separation between the two westward current jets indicates that they may be associated with different processes in the different magnetospheric regions. The intensity of the eastward electrojet and the morningside westward electrojet is mainly controlled by the direct energy input due to solar wind-magnetosphere interaction; whereas the enhancement of the electrojet near local midnight is the manifestation of substorms as a result of sporadic unloading of magnetotail energy [*Clauer and Kamide*, 1985; *Kamide and Baumjohann*, 1993]. The westward edge of the nightside westward electrojet is the location of the westward traveling surge (WTS) [*Akasofu et al.*, 1965; *Kamide and Akasofu*, 1975; *Baumjohann*, 1983]. During the expansion phase, the auroral electrojets on the dawnside and duskside are nearly unchanged. The electrojet near midnight, however, is not only enhanced in its strength but also expanded longitudinally to join with the westward electrojet from the dawnside, as well as to abut with the eastward electrojet from the duskside near 2300 MLT. At the peak of the expansion phase, the nightside electrojet is most intense and at the same time, the dawnside and duskside electrojets are also enhanced. During the recovery phase, all three electrojets gradually decay, and the nightside electrojet retreats to the morning sector.

Figure 4 has shown clearly that the nightside westward electrojet develops separately from the westward electrojet in the late morning sector following the onset of the expansion phase. As the substorm evolves, the nightside electrojet expands longitudinally as well as intensifies at a greater rate than the morning electrojet, which shows no obvious change until at the peak of the expansion phase. During the recovery phase, the nightside electrojet diminishes rapidly but the morning electrojet persists. Owing to the different causes for the two westward electrojets, the former is called the substorm electrojet and the latter the convection electrojet [*Baumjohann*, 1983; *Kamide et al.*, 1994].

Field-aligned current. The field-aligned current density $j_{||}$ is found from the divergence of the horizontal current:

$$j_{||} = \nabla_\perp \cdot (\Sigma_p E) + \nabla_\perp \cdot (\Sigma_H b \times E) \qquad (1)$$

where Σ_p and Σ_H are the height-integrated Pedersen and Hall conductances, respectively, b is a unit vector of the magnetic field, and E is the ionospheric electric field. Thus the field-aligned current depends on the divergence of the electric field as well as the gradient of the conductances. In the AMIE procedure we assume that the magnetic field is vertical and neglect the neutral wind dynamo effect. Figure 5 illustrates the field-aligned-currents' response to the substorm. Solid (dashed) contours represent downward (upward) field-aligned currents with contour intervals of 0.2 $\mu A/m^2$ starting at ± 0.1 $\mu A/m^2$. The total downward field-aligned current given at the upper right is defined as one half the hemispheric integral of the absolute value of the current density over the area poleward of 50°. At 0810 UT, the large-scale distribution shows upward region 1 and downward region 2 currents on the duskside, and downward region 1 and upward region 2 currents on the dawnside, similar to the statistical patterns of *Iijima and Potemra* [1978]. However, unlike the statistical distribution of the field-aligned current which peaks at about 0900 MLT for downward region 1 current and at 1400 MLT for upward region 1 current [*Iijima and Potemra*, 1978], Figure 5a shows double peaks for both dawn and dusk region 1 currents at the onset of the substorm. The duskside upward current peaks at about 1600 and 2200 MLT, and the dawnside downward current peaks at 0800 and 0130 MLT, respectively. In addition, a weak upward current appears poleward of the dawnside region 1 current. Along with the upward region 2 current from the dawnside, they form triple current sheets in the post-midnight sector. However, the polarities of the triple current sheets are opposite to those associated with the Harang discontinuity in the midnight sector [*Iijima and Potemra*, 1978]. The field-aligned currents become more intense as the substorm progresses. The dayside peaks of current density

appear relatively stable; whereas the nightside peaks tend to move counterclockwise. Between 0810 UT and 0840 UT, the nightside peak of the upward current has moved from pre-midnight to post-midnight at about 0200 MLT. It remains at about the same MLT as the downward region 1 current peak throughout the substorm expansion phase as well as at the substorm peaks. During the substorm recovery phase, the intensity of the field-aligned current decreases. The upward current that is poleward of the downward region 1 current in the early morning sector nearly disappears at 1030 UT.

Compared with the horizontal ionospheric current, the field-aligned current distribution is more complicated. In the post-midnight region, the downward region 1 current from the morningside is surrounded by the upward field-aligned currents at the poleward and equatorward edges. Using simultaneous imagery, high-resolution magnetic field, and precipitating particle measurements from the DMSP F7 satellite, *Bythrow and Potemra* [1987] found that the most poleward upward field-aligned current near the head of the WTS corresponds to a narrow discrete auroral arc and the equatorward upward current corresponds to broad and bright auroral emission. The downward field-aligned current in the middle separates the discrete arc at the poleward edge of the WTS from the bright auroral oval of the WTS. They attribute the WTS to the expansion of the central plasma sheet into the plasma sheet boundary layer in the distant magnetotail. *Lyons et al.* [1990] have also related the poleward boundary of the WTS to the separatrix between the open and closed magnetic field lines. Because of the lack of satellite observations in the midnight region during this substorm event, we are unable to examine the magnetospheric origins of the different field-aligned currents associated with the WTS. Furthermore, enhanced upward field-aligned currents are often found at the westward edge of the WTS and the more widespread downward currents in the eastern part [e.g., *Baumjohann et al.*, 1981; *Opgenoorth et al.*, 1983]. This east-west pair of field-aligned currents is fed by the westward substorm electrojet, which forms the substorm current wedge [*McPherron et al.*, 1973]. However, as shown in Figure 5, the pair of field-aligned currents in the post-midnight sector lines up in the north-south direction, instead of in the east-west direction. Because there was no satellite passing over the region near midnight during the substorm to provide valuable information about auroral precipitation, the ionospheric conductances in that region were mainly determined by the statistical models which tend to have a larger gradient in the north-south direction than in the east-west direction. During substorms, the field-aligned currents in the midnight sector are influenced strongly by conductivity enhancements generated by energetic precipitating electrons associated with the WTS.

Joule heating rate. Joule heating is attributed as the main dissipation channel of the magnetospheric energy into the ionosphere [*Lu et al.*, 1995]. As demonstrated by *Richmond and Kamide* [1988], a very important feature of AMIE is its ability to give quantitative information about the error δe associated with the estimated large-scale electric field E at each grid point. Thus the height-integrated Joule heating rate Q_J is estimated by [*Richmond et al.*, 1990]:

$$Q_J = \Sigma_P E^2 + \Sigma_P \langle (\delta e)^2 \rangle \quad (2)$$

Here the second term represents the adjustment in estimated Joule heating rate due to the E-field uncertainty. Figure 6 shows the distribution of the estimated height-integrated Joule heating rate. The total Joule heating rate integrated above 50° magnetic latitude is given at the upper right corner of each pattern. By examining these patterns, it is easy to see that Joule heating is concentrated in the regions of the duskside eastward electrojet, the dawnside westward electrojet, and the nightside westward electrojet. As the substorm progresses, Joule heating becomes more and more intense, especially in the early morning sector. As a comparison, we also estimate the Joule heating rate without taking into account the second term of the above equation for the same six UT times (the patterns are not shown). Though the general distribution is about the same, the magnitude of the total hemisphere-integrated Joule heating rate without the second term is about 10–20% smaller than that using the full expression.

Our procedure for estimating Joule heating rate accounts for uncertainty in the estimation of large-scale ($\sim$ 150 km and greater) electric fields, as discussed by *Richmond et al.* [1990], but does not account for smaller-scale fields or for conductivity uncertainties. Recently, theoretical calculations conducted by *Codrescu et al.* [1995] show that there could be a 30% increase in Joule heating due to small-scale E-field variability. Although neglected conductivity variability will alter the local distribution of Joule heating, it is unlikely to affect the total hemisphere-integrated Joule heating significantly because of cancellations between localized enhancement and reduction in conductivity.

Joule heating represents the major magnetospheric energy dissipation in the ionosphere and thermosphere. Our results indicate that, during the substorm expansion phase, the WTS becomes the primary energy dissipation source because of the Cowling effect [*Baumjohann,* 1983]; it can account for about one half of the total hemisphere-integrated Joule heating.

3.2. Variations of Global Ionospheric Electrodynamic Quantities

Global ionospheric quantities, such as the cross-polar-cap potential drop, the hemisphere-integrated Joule heating rate, and the total field-aligned current, represent important features of the electrodynamic states associated with geomagnetic activity. In this subsection we examine these global quantities and their interrelationships.

Figure 7 shows variations of different parameters representing electrodynamic conditions at high latitudes

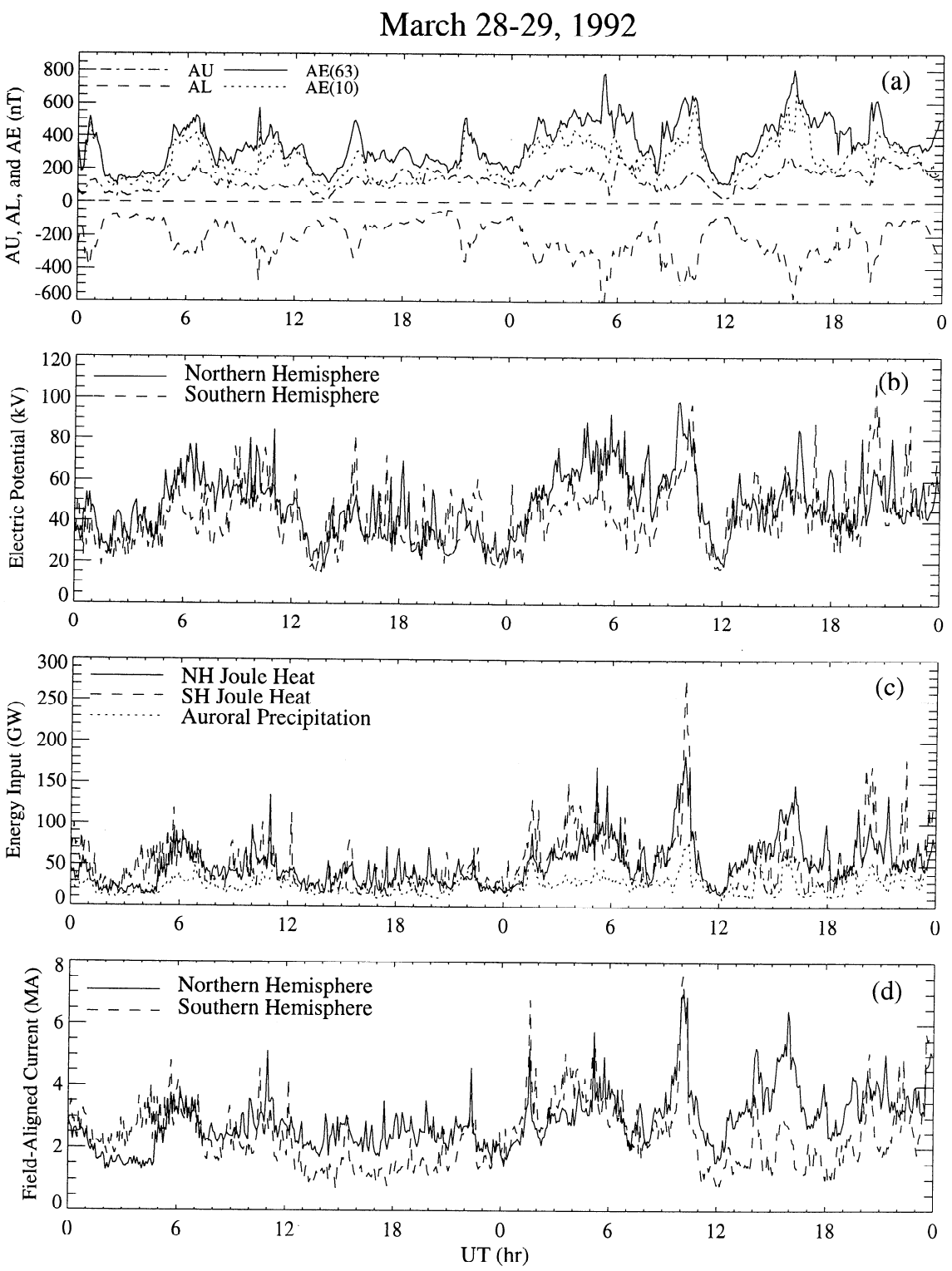

Figure 7. Distribution of various global electrodynamic quantities for the 2-day period of March 28-29, 1992. The spikes in the cross-polar-cap potential drop as well as Joule heating and field-aligned current correspond to the times when the potential drops were determined from the DMSP passes. See the text for more details.

over the period of March 28–29, 1992. The top panel shows the auroral electrojet indices AU (dash-dotted), AL (dashed), and AE (solid) calculated from the north-south component of the magnetic perturbations measured by 63 ground stations between 55° and 76° magnetic latitudes north and south. As a comparison, the dotted line in the top panel represents the AE index calculated from 10 out of the 12 standard AE stations

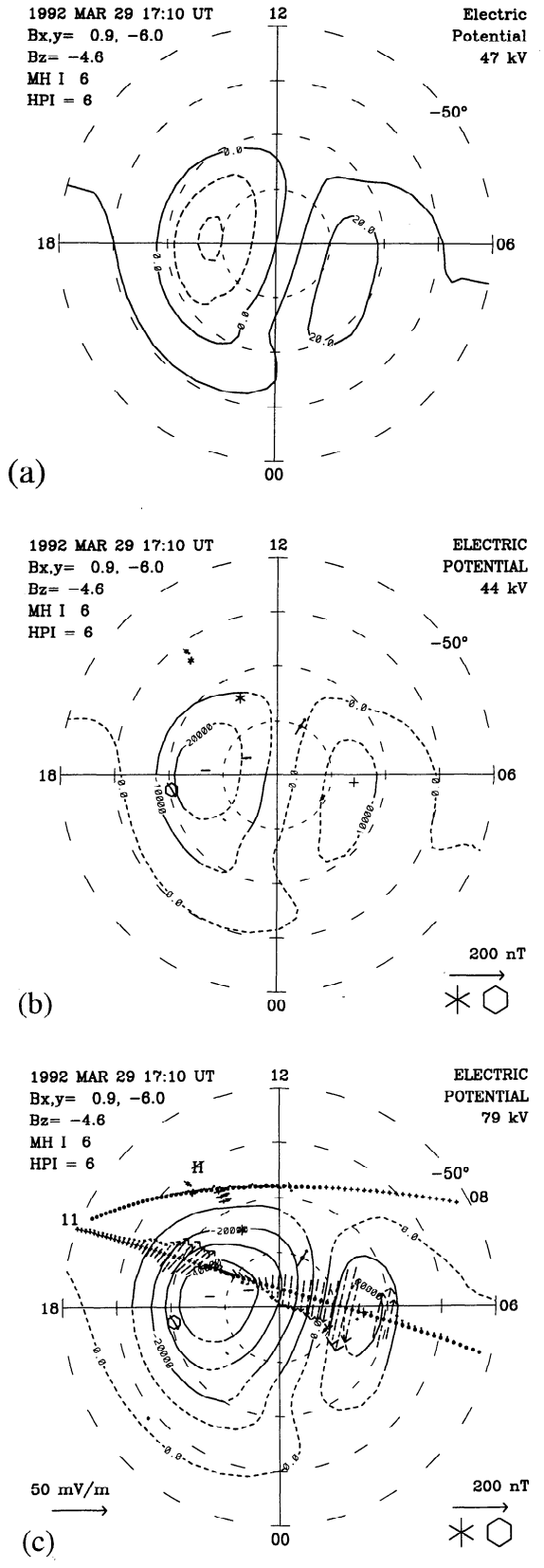

Figure 8. (a) The statistical convection pattern corresponding to HPI=6 at 1710 UT on March 29, 1992. (b) The AMIE convection pattern derived from ground magnetometer data only. (c) The convection pattern derived from both ground and satellite data.

that were available for this study. The "standard" AE index (i.e., $AE(10)$ in this case) monitors reasonably well the substorm activity during these two moderately disturbed days, but the averaged value of $AE(10)$ is about 28% smaller than the "true" AE index (i.e., $AE(63)$). AL and AE indicate that there are about 10 moderate substorms during this 2-day period. The second panel shows the distribution of the cross-polar-cap potential drop in the northern (solid) and southern (dashed) hemispheres. The potential drops in the two hemispheres are generally comparable, indicating that the IMF is likely to be southward or weakly northward, as evident during the 1320 to 1945 UT interval on March 29. It should be noted that the accuracy of the ionospheric convection estimated from AMIE is determined by the underlying data coverage. The most reliable measurements of the cross-polar-cap potential are from the perpendicular-to-track ion drifts or along-track electric field measurements from near dawn-dusk polar orbiting satellites, such as the DMSP F8 and F11 spacecraft. AMIE tends to underestimate the potential drop when there is a lack of satellite electric field or ion drift measurements for periods of southward IMF. In fact, the spikes of potential drop shown in the second panel of Figure 7 correspond to the intervals of DMSP overflights. We find that, for this equinox period, the cross-polar-cap potential drop without the satellite data is usually about 20–30% lower than that with the satellite data. Since the ground magnetometer coverage is sparse in the southern hemisphere, on a few occasions, the difference in potential drops with and without the satellite data can be as high as 50%. Figure 8 shows one such case, where Figure 8a is the statistical pattern of *Foster et al.* [1986] corresponding to a hemispheric power index of 6, Figure 8b is the pattern derived from ground magnetometer data only, and Figure 8c is the pattern derived from both ground and satellite data. With the ground magnetometer data only, the pattern tends to resemble the statistical model applied, and the resulting cross-polar-cap potential drop is 44 kV. By incorporating the satellite ion drift data into AMIE, both dawn and dusk cells are enhanced, and the potential drop increases to 79 kV.

The third panel in Figure 7 shows the hemispheric integrals of the estimated Joule heating in the northern and southern hemispheres as well as the incident auroral electron energy flux. The total auroral energy input due to precipitating electrons in the two hemispheres is about the same, because conjugate observations have been used in the fitting. Although energetic particle precipitation can become a locally dominant dissipation source, particularly within the auroral arcs [*Evans et al.*, 1977; *Vickrey et al.*, 1982; *Kelley et al.*, 1991], it is globally less significant than Joule heating. During the 2 days, the average value of hemisphere-integrated Joule heating rate is 51 GW, and the average value of the hemisphere-integrated auroral energy precipitation rate is about 26 GW. So the hemispheric auroral energy dissipation is about one half of the hemi-

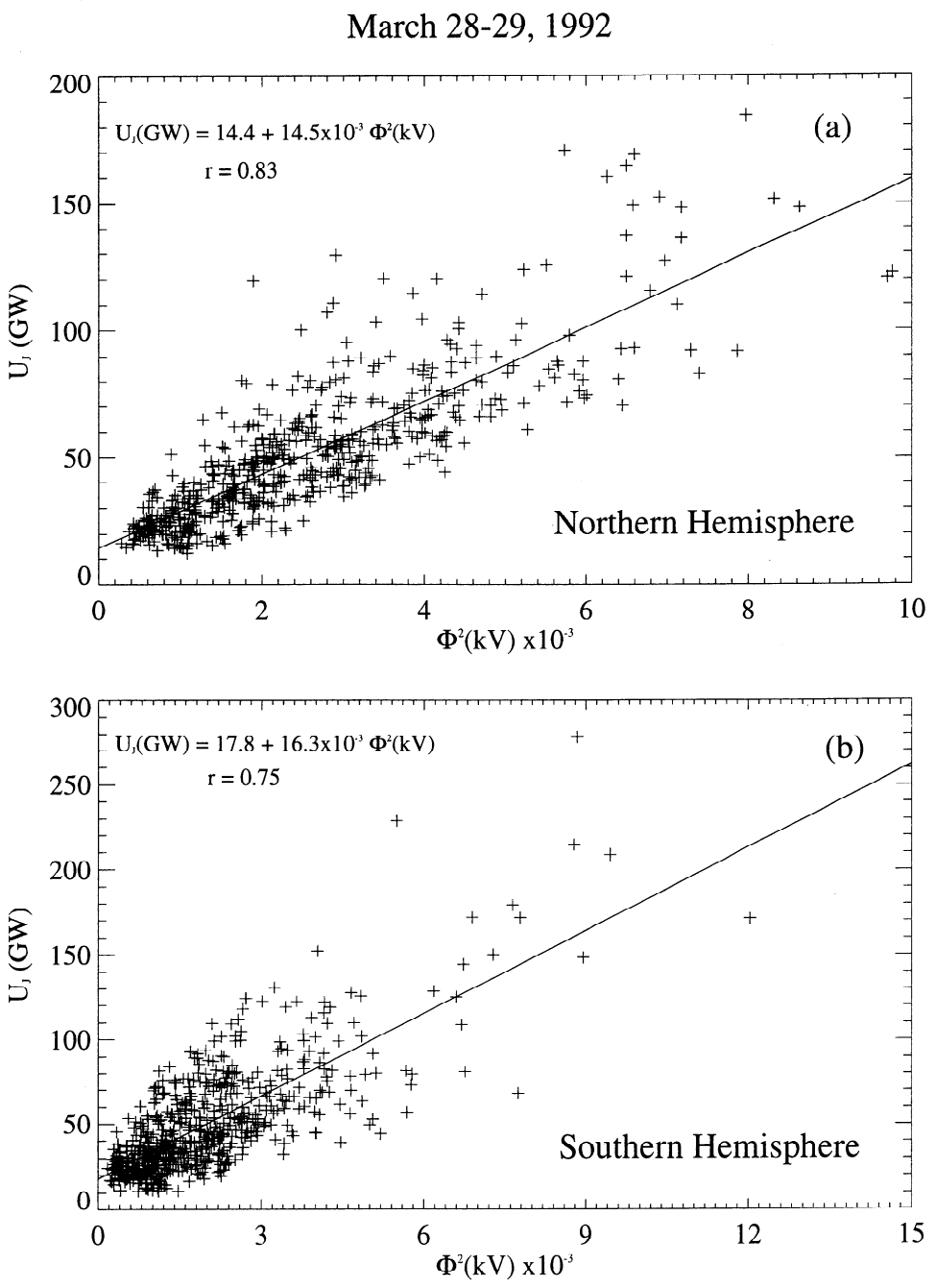

Figure 9. Scatter plots of hemisphere-integrated Joule heating U_J versus the cross-polar-cap potential Φ squared in the (a) northern and (b) southern hemispheres. The solid line shows a linear regression fit.

spheric integrated Joule heating rate. It is noted that the Joule heating estimated from AMIE in this study is about 50% smaller than the "convection heating" (e.g., without taking into account the neutral winds) estimated from the TIGCM in the previous study [*Lu et al.*, 1995]. One of the causes for the discrepancy is the way that ionospheric conductivity is calculated. The AMIE procedure adopts the empirical formulas of *Robinson et al.* [1987], whereas the TIGCM calculates ionospheric conductivities through the self-consistent estimates of electron and ion densities and temperatures within the model. It is found that, over the auroral regions, the height-integrated Pedersen conductivity from the TIGCM is about 30% larger than that of AMIE, but the height-integrated Hall conductivity is about the same. It should be emphasized here that the AMIE procedure neglects the neutral wind dynamo. From the TIGCM simulations, *Lu et al.* [1995] found that the neutral winds can have a significant influence on the ionospheric electrodynamics by reducing the total Joule heating by approximately 28%.

Harel et al. [1981] have derived an empirical relation between the hemisphere-integrated Joule heating rate U_J and the cross-polar-cap potential drop Φ:

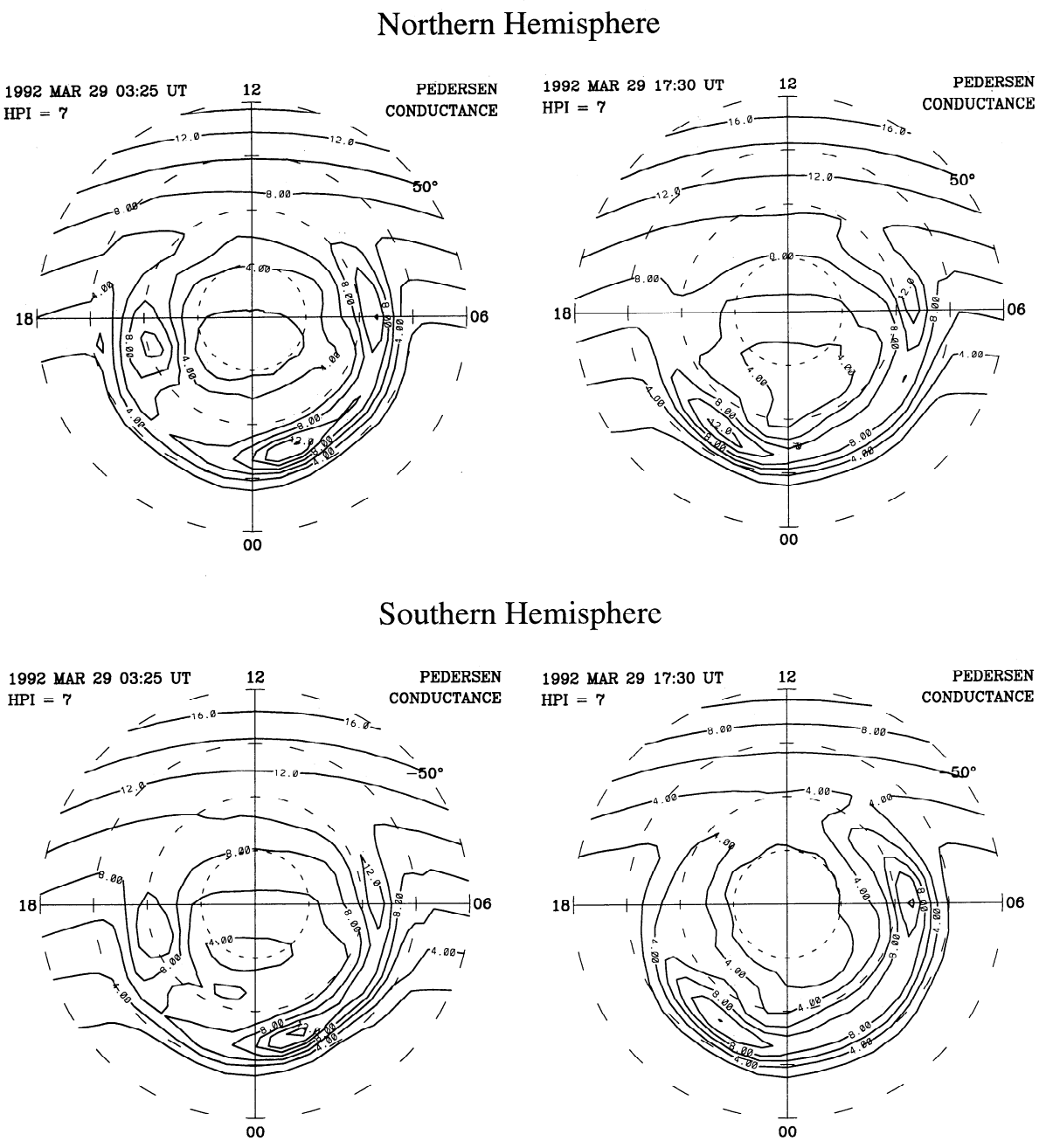

Figure 10. Height-integrated Pedersen conductances derived at 0325 UT and 1730 UT on March 29, respectively. The northern hemispheric patterns are on the top, and the southern hemispheric patterns on the bottom. The contour intervals are 2 S.

$$U_J = \Sigma_{eff}\Phi^2 \tag{3}$$

where Σ_{eff} is an effective ionospheric Pedersen conductance, which is about 30 Siemens (S) from their study. To follow this idea, Figure 9 is the plot of U_J versus Φ^2, with a correlation coefficient of 0.83 in the northern hemisphere (top), and 0.75 in the southern hemisphere (bottom). The obtained effective conductance is 14.5 S in the northern hemisphere and 16.3 S in the southern hemisphere, which is about half of the magnitude derived by *Harel et al.* [1981].

The bottom panel of Figure 7 is the hemisphere-integrated field-aligned current $J_{\|}$ in the northern (solid) and southern (dashed) hemispheres. The field-aligned current in the southern hemisphere is larger than that in the northern hemisphere between about 0300 and 0500 UT on both days, when the south magnetic pole is toward the Sun. Between about 1300 and 2200 UT, the field-aligned current in the northern hemisphere is larger than that in the southern hemisphere. The difference in field-aligned current between the two hemispheres can be attributed to the asymmetry of the iono-

spheric conductivity due to the hemispheric asymmetry in deposition of solar irradiation. Figure 10 shows the height-integrated Pedersen conductivities in the northern (top) and southern (bottom) hemispheres derived at 0325 and 1730 UT on March 29, 1992. At 0325 UT, the terminator of the solar-induced conductivity is about 10° nightside of the dawn-dusk meridian in the northern hemisphere, and about 30° in the southern hemisphere. In contrast, at 1730 UT, the northern magnetic pole is toward the Sun; the terminator is about 30° nightside of the dawn-dusk meridian in the northern hemisphere and about 10° dayside of the dawn-dusk meridian in the southern hemisphere. The offset of the magnetic pole from the geographic pole introduces a diurnal variation of ionospheric conductivity, even during equinoxes. In the auroral zone, the conductivities are produced by both auroral precipitation and solar irradiation. The auroral-produced conductivities are nearly the same in the two hemispheres because conjugate observations have been used; whereas the solar EUV-produced conductivities in the auroral zones have a difference of about 30% between the two hemispheres at these two UT times. Such hemispheric differences are also apparent in the hemisphere-integrated Joule heating for the same reason, and similarly in estimates of the Joule heating rate in the TIGCM where neutral winds are included (*Emery et al.* [this issue]).

As illustrated in Figure 7, the cross-polar-cap potential drop, the hemispheric integrated Joule heating rate, and the total field-aligned current are apparently correlated with *AE*. To further examine the interrelationships among the various global quantities, Figure 11 shows the scatter plots of the different quantities versus the *AE* index (i.e., *AE*(63)) in both northern and southern hemispheres. Each panel also lists the linear correlation coefficient, the average value, and the linear fitting of each quantity to *AE*. Overall, the correlation coefficient r in the southern hemisphere is smaller than that in the northern hemisphere. This is because only 3 of the 63 ground magnetometer stations contributing to the calculation of the auroral indices are in the southern hemisphere. Therefore, the auroral indices presented in this study mainly reflect geomagnetic activity in the northern hemisphere. Additionally, the ground data coverage in the southern hemisphere is poorer than that in the northern hemisphere. The average values of the three global quantities over the 2-day period are nearly comparable between the two hemispheres, and this is consistent with the fact that this period is in an equinox season. From the linear regression fit, the proportionality factor between Φ and *AE* is 0.08 kV/nT in the northern hemisphere and 0.07 kV/nT in the southern hemisphere, while the proportionality factor between $J_{\parallel}$ and *AE* is 0.005 MA/nT in the northern hemisphere and 0.004 MA/nT in the southern hemisphere. These proportionality factors are about 30% smaller than those given by *Richmond et al.* [1990]. Note that *Richmond et al.* [1990] adopted *AE*(12) in their study while we used *AE*(63). If we had used the "standard" *AE* (i.e., *AE*(10)) which is about 28% smaller than *AE*(63), our results would be nearly the same as *Richmond et al.* [1990]. Previous studies have resulted in a proportionality factor of U_J versus *AE* between 0.21 GW/nT and 0.33 GW/nT [*Richmond et al.*, 1990; *Ahn et al.*, 1983a; *Baumjohann and Kamide*, 1984]. As a comparison, the proportionality factor derived from this study is somewhat smaller: 0.16 GW/nT in the northern hemisphere and 0.13 GW/nT in the southern hemisphere. The reason for such discrepancy between these independent studies is complicated, but it may be attributed to the fact that different *AE* index (for example, *AE*(12) of A. D. Richmond et al.; *AE*(71) of B.-H. Ahn et al. and W. Baumjohann and Y. Kamide; and *AE*(61) for this study) and different conductivities (empirical conductivity models of B.-H. Ahn et al. and W. Baumjohann and Y. Kamide, and AMIE-derived conductivities of A. D. Richmond et al. and this study) are used for different studies. Seasonal effect may also contribute to the discrepancy.

3.3. Estimate of the Ring Current Injection Rate

In addition to the energies dissipated into the high-latitude ionosphere, mainly through Joule heating and auroral precipitation, energy that has been stored in the magnetotail is partially converted into particle energy in the ring current after the onset of a geomagnetic storm. A sophisticated calculation of the ring current energy injection rate is rather complicated, which would require detailed information about the dynamic properties of the inner magnetosphere. Unfortunately, such information is not available during this period due to the lack of good satellite coverage in the magnetosphere. In this study, we estimate the ring current injection rate by using an empirical formula.

The solid line in Figure 12a is the standard 1-hour D_{st} (the provisional data from the World Data Center-C2 at Kyoto University, Japan) which has been linearly interpolated to 5-min resolution. As a comparison, the dashed line shows the 5-min D_{st} index from the measurements of 11 stations located equatorward of ±45° magnetic latitude. The standard D_{st} represents well the low-frequency variation, while the measured D_{st} shows more high-frequency structures.

The ring current injection rate U_R (in centimeter-grams-seconds units) can be calculated according to *Akasofu* [1981]:

$$U_R = 4 \times 10^{20} \left(\frac{\partial \bar{D}_{st}}{\partial t} + \frac{\bar{D}_{st}}{\tau_R} \right) \tag{4}$$

where τ_R in seconds is the ring current particle lifetime, and $\bar{D}_{st}$ in nT is the pressure-corrected D_{st} index defined by [*Zwickl et al.*, 1987]

$$\bar{D}_{st} = |D_{st}| - D_{st}(P) \tag{5}$$

with $D_{st}(P) = aP^{1/2} - b$, $a = 0.2$ nT/(eV cm^{-3})$^{1/2}$, $b = 20$ nT, and P is defined as the solar wind dynamic pressure. During the interval of 1320-1930 UT on March 29, the available solar wind plasma data indicate a so-

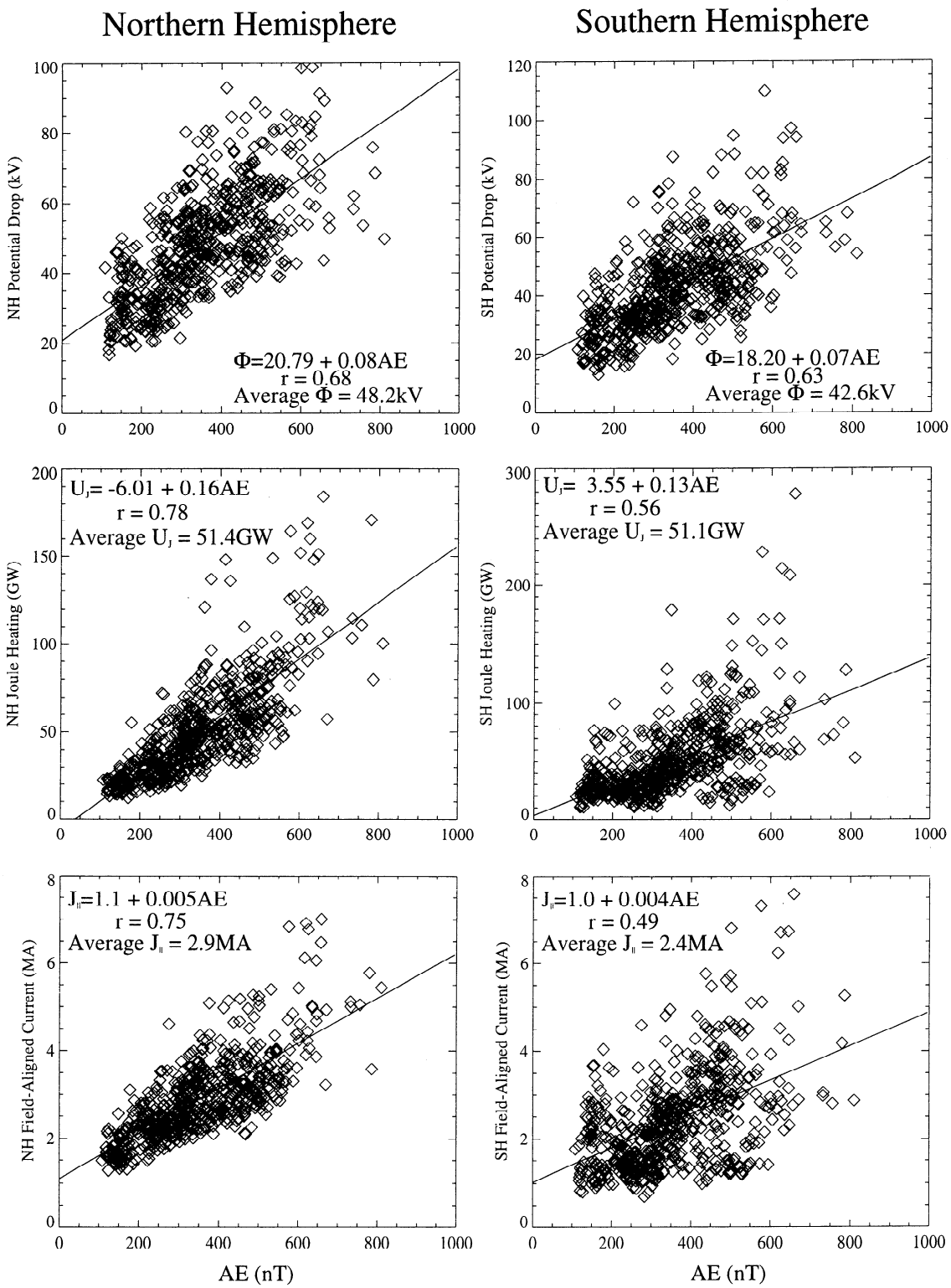

Figure 11. (top to bottom) Scatter plots of the cross-polar-cap potential drop, hemisphere-integrated Joule heating, and hemisphere-integrated field-aligned current versus AE. The northern hemisphere is on the left, and the southern hemisphere on the right.

lar wind pressure of $16 \times 10^3 \mathrm{eV/cm^3}$, corresponding to $D_{st}(P)$ of 5 nT. We assume that the solar wind pressure is constant for the entire 2-day period. The ring current energy injection rate depends on τ_R, which is a highly uncertain parameter that varies from less than 1 hour to about 20 hours [e.g., *Akasofu*, 1981; *Zwickl et al.*, 1987], depending on the solar wind energy transfer rate ϵ. In Figure 12b, the dashed and solid lines are the ring current injection rate U_R corresponding to τ_R = 3.5 hours and 20 hours, respectively, using the

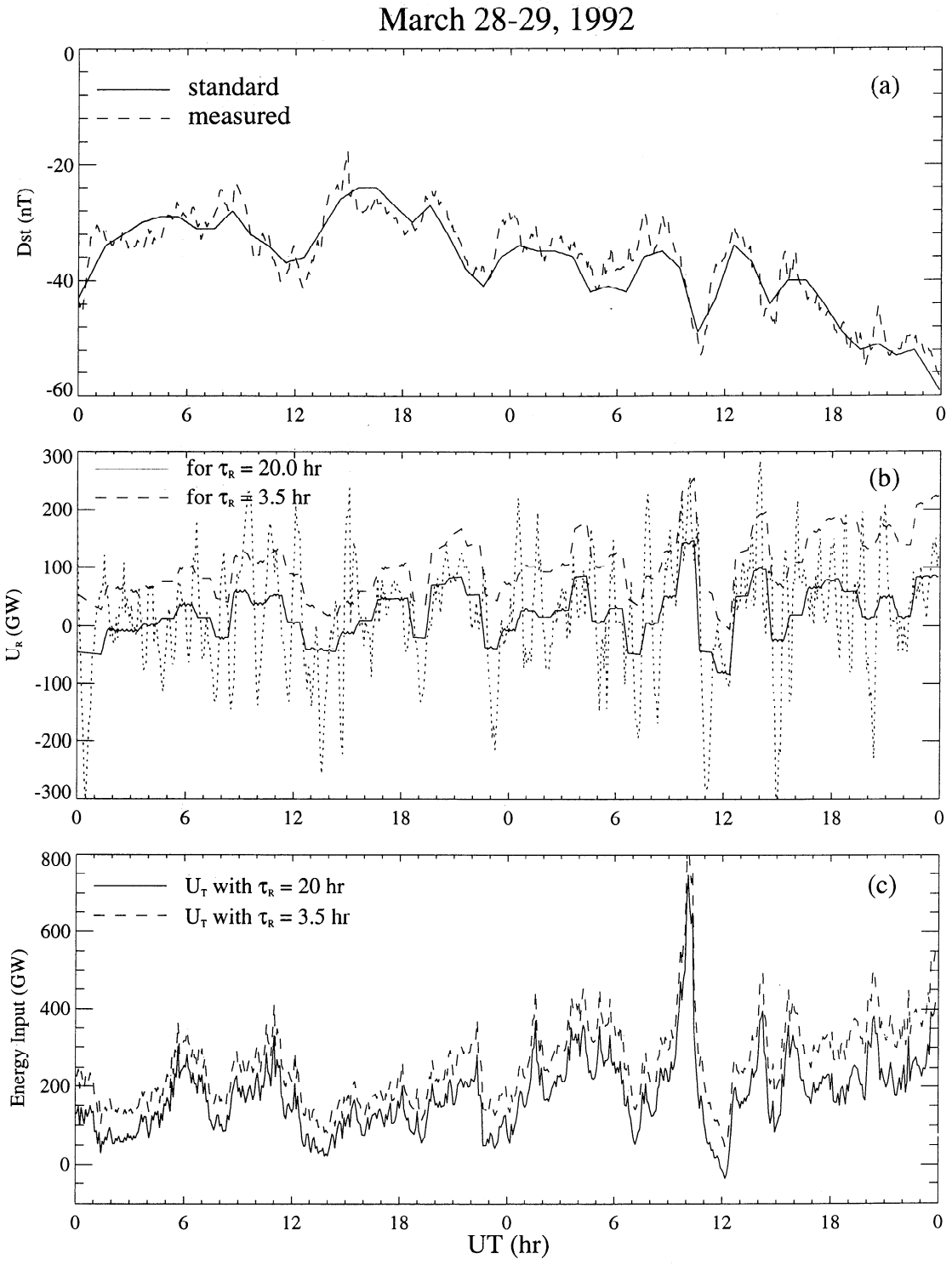

Figure 12. (a) The solid line shows the standard 1-hour D_{st} (previsional data), and the dashed line shows the measured D_{st} derived from 5-min averaged data from 11 stations located between $\pm 40°$ magnetic latitude. (b) The solid and dashed lines are the ring current injection rates corresponding to $\tau_R = 3.5$ hours and $\tau_R = 20$ hours, respectively, using the standard D_{st}. The dotted line is the ring current injection corresponding to $\tau_R = 20$ hours, using the measured D_{st}. (c) The total magnetospheric energy inputs corresponding to $\tau_R = 3.5$ hours (dashed line) and $\tau_R = 20$ hours (solid line).

standard D_{st} values. Choosing $\tau_R = 3.5$ hours ensures that U_R is always larger than zero. Alternatively, since ϵ is less than 5×10^{18} ergs/s during the interval when the solar wind data are available (see Figure 13), one can also take $\tau_R = 20$ hours [*Akasofu*, 1981]. Choosing $\tau_R = 20$ hours, however, makes U_R became negative at several intervals. This implies that τ_R should be a time-dependent parameter that varies between 3.5 and

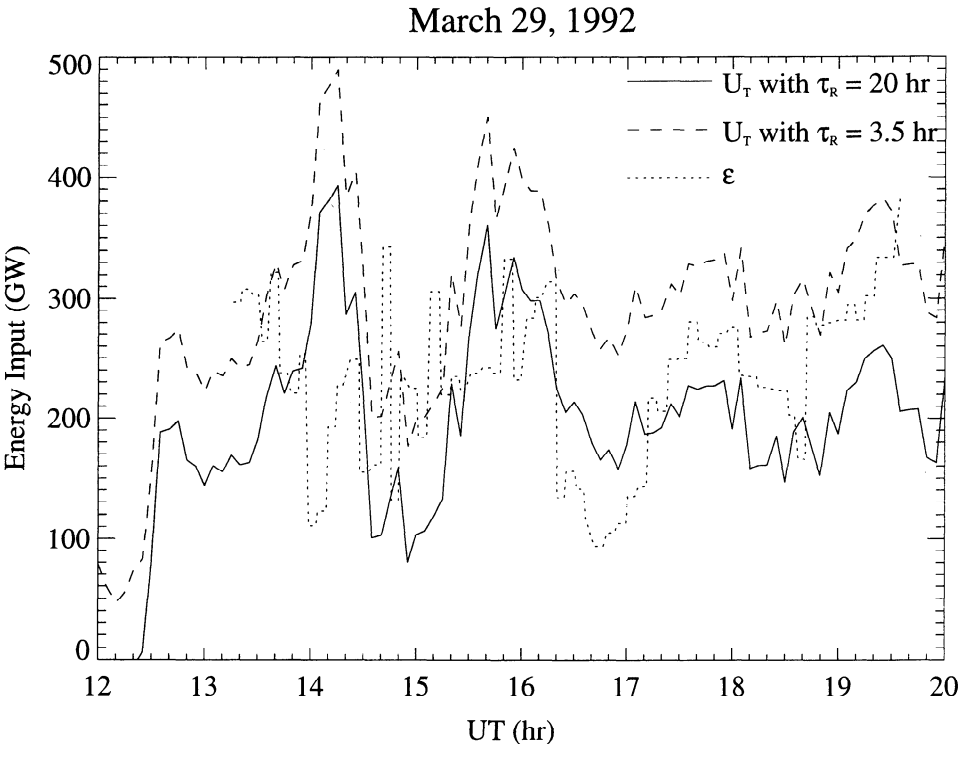

Figure 13. Comparison of the solar wind energy transfer rate ϵ (dotted line) and the total magnetospheric energy input U_T for $\tau_R = 3.5$ hours (dashed line) and $\tau_R = 20$ hours (solid line).

20 hours, rather than a constant during this 2-day period, even though the D_{st} index is relatively steady. The average value of U_R is 124 GW (or 1.24×10^{18} ergs/s) for $\tau_R = 3.5$ hours and 85 GW for $\tau_R = 20$ hours. The dotted line represents the ring current injection rate corresponding to $\tau_R = 20$ hours, using the measured D_{st}, which shows some superimposed fine structures. Figure 12c shows the total magnetospheric energy input U_T, which is the sum of Joule heating and auroral energy precipitation in both hemispheres and the ring current injection rate U_R. The solid line corresponds to $\tau_R = 20$ hours and the dashed line for $\tau_R = 3.5$ hours.

3.4. Estimate of the Solar Wind Energy Transfer Rate

The solar wind is the ultimate energy source which is responsible for virtually all electrodynamic processes in the magnetosphere. Only a small fraction of solar wind kinetic energy is transmitted into the magnetosphere, and the energy transfer rate from the solar wind to the magnetosphere is largely controlled by the IMF orientation [*Perreault and Akasofu*, 1978; *Akasofu*, 1981]. The energy transfer rate is given in Gaussian units by [*Perreault and Akasofu*, 1978]

$$\epsilon = \nu B^2 \sin^4\left(\frac{\theta}{2}\right) l_0^2 \qquad (6)$$

where ν is the solar wind speed, B is the interplanetary magnetic field, θ is the angle between the z direction and the projection of the IMF in the $y-z$ plane of the GSM coordinate system, and $l_0 = 7\ R_E$ corresponding to an effective magnetospheric width of 10 R_E [*Perreault and Akasofu*, 1978]. Plotted in Figure 13 are U_T and ϵ. During this 6-hour interval, the average ϵ is slightly larger than U_T with $\tau_R = 20$ hours, but about half of U_T with $\tau_R = 3.5$ hours. Therefore, in order to match ϵ with U_T, either τ_R should be 20 hours or larger, or l_0 should be increased from 7 R_E to 10 R_E (corresponding to an effective magnetospheric width of about 14.3 R_E). For this case, the latter condition seems more reasonable since it is consistent with the statistical magnetopause configuration of *Sibeck et al.* [1991] for the given IMF values. It should also be pointed out that, in addition to U_T, part of the solar wind energy input ϵ is stored in the magnetotail as well as contributing to plasma sheet heating. Unfortunately, we are unable to quantify this part of energy loss for this particular period. Previous studies [*Weiss et al.*, 1992, and references therein] indicate that typical values of energy storage in the magnetotail and plasma sheet heating are about 5×10^{11}W and 1×10^{11}W, respectively.

The solar wind energies are transmitted to the magnetosphere and ionosphere through magnetic coupling. It is of interest to estimate the coupling efficiency between the solar wind and the magnetosphere by comparing the solar wind energy input with the energy dissipation into the magnetosphere. During the 6-hour interval, the average B_z is about -4 nT, which implies a corresponding dawn meridian magnetopause distance of 14.5 R_E [*Sibeck et al.*, 1991]. Thus the effective cross-sectional area of the magnetopause is about 3×10^{20}cm^2.

Given the average solar wind speed of 350 km/s and density of 12 amu/cm^3, the solar wind energy input U_{SW} is about 1×10^{20}erg/s or 1×10^4GW. Therefore, the coupling efficiency, defined as the ratio of U_T over U_{SW}, is about 0.03. This value is approximately 1 order larger than that during strong northward IMF conditions [e.g., *Tsurutani and Gonzalez*, 1995].

4. Summary

We have presented in this paper the large-scale high-latitude ionospheric electrodynamics during the ATLAS/GEM period of March 28–29, 1992. The high-latitude auroral precipitation, plasma convection, and other related electrodynamic quantities are important to the thermospheric dynamics in terms of ion drag and Joule heating. This work can be summarized as follows:

1. The 2-day campaign period is characterized by several moderate substorms. Examination of the large-scale patterns of various electrodynamic fields associated with the different phases of a substorm reveals the following features: (a) Distributions of the ionospheric convection show clearly the coexistence of double positive potential peaks during the expansion phase of the substorm: one peak is located near 0300 MLT, the other near dawn. During the recovery phase, the peak potential in the early morning sector gradually decreases. (b) At the onset of the substorm, there are three distinctive ionospheric electrojets: the eastward electrojet on the duskside; the westward electrojet in the postdawn sector; and the westward electrojet in the post-midnight sector, that is, the substorm electrojet. As the substorm progresses, the substorm electrojet not only is enhanced in its strength but also expands longitudinally toward both dawn and dusk. On the other hand, the dawn and dusk convection electrojets are much slower in response to the development of the substorm. No significant enhancement of these electrojets is seen until the peak of the substorm. As the substorm subsides, the substorm electrojet gradually decays and eventually merges with the dawnside convection electrojet. (c) During the expansion phase, the distribution of field-aligned current shows that the downward current sheet is surrounded by upward currents poleward and equatorward in the vicinity of the WTS, and the current density is intensified. During the recovery phase, the field-aligned currents tend to die away, especially the most poleward component. (d) Ionospheric Joule heating is concentrated in the regions associated with auroral electrojets. During substorms, the WTS becomes the primary energy dissipation source due to the Cowling effect.

2. Variations of global ionospheric quantities, such as the cross-polar-cap potential drop, the hemisphere-integrated Joule heating, and the total field-aligned current, represent important electrodynamic features associated with geomagnetic activity. A reasonably good correlation has been found between the various global quantities and the AE index, with a correlation coefficient between 0.5 and 0.8. In this study, we have calculated the AE index from ground magnetic perturbations observed by 63 stations that are located between 55° and 76° magnetic latitudes north and south. The AE index thus obtained (i.e., $AE(63)$) is the most accurate one possible for this particular period, and it is larger than the standard AE index by 28% on the average over the 2 days.

3. On the average over this 2-day period, the total globally integrated Joule heating rate, summed over the two hemispheres, is about 102 GW, and the total globally integrated auroral energy precipitation rate is about 52 GW. This implies that although auroral energy precipitation can be locally important, it is globally less significant then Joule heating. As indicated by the AE index, this 2-day period is featured by several moderate substorms and the AE index never exceeds 800 nT. The average value of the Joule heating rate derived from this study is rather moderate, which is consistent with the moderate geomagnetic activity level during these 2 days. Individual event studies have reported estimates of the Joule heating rate between 10 GW (or 10^{10} W) and 1000 GW (or 10^{12} W) [e.g., *Baker et al.*, 1985; *Richmond et al.*, 1990; *Cooper et al.*, 1995], depending on geomagnetic activity.

4. Using an empirical formula, we have estimated the ring current energy injection rate to be 125 GW for a decay time of 3.5 hours, and 85 GW for a decay time of 20 hours. In this study, we also estimate an energy-coupling efficiency of 3% between the solar wind and the magnetosphere when the IMF B_z is southward.

Acknowledgments. We wish to acknowledge the Coupling, Energetics and Dynamics of Atmospheric Regions (CEDAR) Database at the National Center for Atmospheric Research (NCAR) for providing the Sondrestrom incoherent scatter radar data. Both facilities are supported by the National Science Foundation (NSF). The Johns Hopkins University Applied Physics Laboratory HF radar at Goose Bay, Labrador, is supported in part by the NSF Division of Atmospheric Sciences under NSF grant ATM-9003860 and in part by the National Aeronautics and Space Administration (NASA) under grant NAG5-1099. The Wick radar was operated and maintained by the Department of Physics and Astronomy at the University of Leicester in United Kingdom. We thank L. Morris at the World Data Center for selecting the ground magnetometer data, the Canadian Space Agency and T. Hughes at the National Research Council of Canada for providing data from the CANOPUS magnetometer array, E. Friis-Christensen at the Danish Meteorological Institute for distributing the Greenland magnetometer network data, and O. Troshichev for delivering the Russian Arctic and Antarctic analog data. We also thank the Technical University of Braunchweig and the Finnish Meteorological Institute for supplying IMAGE magnetometer network data, the Auroral Observatory at the University of Tromso, Norway, for contributing data from the Norwegian Arctic Stations, P. Sutcliffe at the Hermanus Magnetic Observatory in South Africa for submitting the Hermanus magnetometer data, C. G. Maclennan at AT&T Bell Laboratories for providing data from their ground stations at Iqaluit (FRB) in Canada, and at McMurdo (MCM) and South Pole (SPA) in the Antarctic. We are grateful to F. Rich for providing us the DMSP data, the IMP 8 magnetometer data processing team at the Laboratory for Extraterrestrial Physics of GSFC for the use of the IMP 8 IMF data, and A. Lazarus at MIT

for the IMP 8 plasma data. The Exos D satellite data were provided by A. Mutsuoka and H. Hayakawa at the Institute of Space and Astronautical Science, and by T. Nagatsuma and H. Fukunishi at the Upper Atmosphere and Space Research Laboratory of Tohoku University, Japan. We thank S. Nguyen and C. A. Gonzalez for their efforts with the UARS data. We also thank A. Richmond, E. Szuszczewicz, M. Codrescu, and T. Fuller-Rowell for many helpful comments and fruitful discussions. This study was supported in part by NSF under grant 93-SFA.1 and by NASA contract NAS5-27753 with SWRI.

The Editor thanks R. M. Robinson and A. G. Burns for their assistance in evaluating this paper.

References

Ahn, B. -H., S. -I. Akasofu, and Y. Kamide, The Joule heat production rate and the particle energy injection rate as a function of the geomagnetic indices *AE* and *AL*, *J. Geophys. Res., 88,* 6275, 1983a.

Ahn, B. -H., R. M. Robinson, Y. Kamide, and S. -I. Akasofu, Electric conductivities, electric fields and auroral energy injection rate in the auroral ionosphere and their empirical relations to the horizontal magnetic disturbances, *Planet. Space Sci., 31,* 641, 1983b.

Akasofu, S.-I., Energy coupling between the solar wind and the magnetosphere, *Space Sci. Rev., 28,* 121, 1981.

Akasofu, S.-I., D. S. Kimball, and C.-I. Meng, The dynamics of the aurora II. Westward traveling surges, *J. Atmos. Terr. Phys., 27,* 173, 1965.

Baker, D. N., T. A. Fritz, R. L. McPherron, D. H. Fairfield, Y. Kamide, and W. Baumjohann, Magnetotail energy storage and release during the CDAW 6 substorm analysis intervals, *J. Geophys. Res., 90,* 1205, 1985.

Baumjohann, W., Ionospheric and field-aligned current system in the auroral zone: A concise review, *Adv. Space Res., 2,* 55, 1983.

Baumjohann, W., and Y. Kamide, Hemispherical Joule heating and the *AE* indices, *J. Geophys. Res., 89,* 383, 1984.

Baumjohann, W., R. J. Pellinen, H. J. Opgenoorth, and E. Nielsen, Joint two-dimensional observations of ground magnetic and ionospheric electric fields associated with auroral zone currents: Current systems associated with local auroral break-ups, *Planet. Space Sci., 29,* 431, 1981.

Bythrow, P. F., and T. A. Potemra, Birkeland currents and energetic particles associated with optical auroral signatures of a westward traveling surge, *J. Geophys. Res., 92,* 8691, 1987.

Chenette, D. L., D. W. Datlowe, R. M. Robinson, T. L. Schumaker, R. R. Vondrak, and J. D. Winningham, Atmospheric energy input and ionization by energetic electrons during the geomagnetic storm of 8-9 November 1991, *Geophys. Res. Lett., 20,* 1323, 1993.

Clauer, C. R., and Y. Kamide, DP 1 and DP 2 current systems for March 22, 1979 substorm, *J. Geophys. Res., 90,* 1343, 1985.

Codrescu, M. V., T. J. Fuller-Rowell, and J. C. Foster, On the importance of E-field variability for Joule heating in the high-latitude thermosphere, *Geophys. Res. Lett., 22,* 2393, 1995.

Cooper, M. L., C. R. Clauer, B. A. Emery, A. D. Richmond, and J. D. Winningham, A storm time assimilative mapping of ionospheric electrodynamics analysis for the severe geomagnetic storm of November 8-9, 1991, *J. Geophys. Res., 100,* 19,329, 1995.

Crowley, G., B. A. Emery, R. G. Roble, H. C. Carlson, Jr., and D. J. Knipp, Thermospheric dynamics during September 18-19, 1984, 1, Model simulations, *J. Geophys. Res., 94,* 16,925, 1989.

Deng, W., T. L. Killeen, A. G. Burns, R. G. Roble, J. A. Slavin, and L. E. Wharton, The effects of neutral inertia on ionospheric currents in the high-latitude thermosphere following a geomagnetic storm, *J. Geophys. Res., 98,* 7775, 1993.

Emery, B. A., et al., Assimilative mapping of ionospheric electrodynamics in the thermosphere-ionosphere general circulation model comparisons with global ionospheric and thermospheric observations during the GEM/SUNDIAL period of March 28-29, 1992, *J. Geophys. Res.,* this issue.

Evans, D. S., N. C. Maynard, J. Troim, T. Jacobsen, and A. Egeland, Auroral vector electric field and particle comparisons, 2, Electrodynamics of an arc, *J. Geophys. Res., 82,* 2235, 1977.

Forbes, J. M., and M. Harel, Magnetosphere-thermosphere coupling: An experiment in interactive modeling, *J. Geophys. Res., 94,* 2631, 1989.

Foster, J. C., J. M. Holt, R. G. Musgrove, and D. S. Evans, Ionospheric convection associated with discrete levels of particle precipitation, *Geophys. Res. Lett., 13,* 656, 1986.

Fukunishi, H., et al., Magnetic field observations of Akebono (EXOS-D) satellite, *J. Geomagn. Geoelectr., 42,* 385, 1990.

Fuller-Rowell, T. J., and D. S. Evans, Height-integrated Pedersen and Hall conductivity patterns inferred from the TIROS-NOAA satellite data, *J. Geophys. Res., 92,* 7606, 1987.

Harel, M., R. A. Wolf, R. W. Spiro, P. H. Reiff, and C.-K. Chen, Quantitative simulation of a magnetospheric substorm, 2, Comparison with observations, *J. Geophys. Res., 86,* 2242, 1981.

Hayakawa, H., et al., Electric field measurement on the Akebono (EXOS-D) satellite, *J. Geomagn. Geoelectr., 42,* 371, 1990.

Iijima, T., and T. A. Potemra, Large-scale characteristics of field-aligned currents associated with substorms, *J. Geophys. Res., 83,* 599, 1978.

Kamide, Y., and S.-I. Akasofu, The auroral electrojet and global auroral features, *J. Geophys. Res., 25,* 3585, 1975.

Kamide, Y., and W. Baumjohann, *Magnetosphere-Ionosphere Coupling,* Springer-Verlag, New York, 1993.

Kamide, Y., et al., Ground-based studies of ionospheric convection associated with substorm expansion, *J. Geophys. Res., 99,* 19,451, 1994.

Kelley, M. C., D. J. Knudsen, and J. F. Vickrey, Poynting flux measurements on a satellite: A diagnostic tool for space research, *J. Geophys. Res., 96,* 201, 1991.

Killeen, T. L., P. B. Hays, G. R. Carignan, R. A. Heelis, W. B. Hanson, N. W. Spencer, and L. H. Brace, Ion-neutral coupling in the high-latitude *F* region: Evaluation of ion heating terms from Dynamics Explorer 2, *J. Geophys. Res., 89,* 7495, 1984.

Lu, G., A. D. Richmond, B. A. Emery, and R. G. Roble, Magnetosphere-ionosphere-thermosphere coupling: Effect of neutral winds on Joule heating and field-aligned current, *J. Geophys. Res., 100,* 19,643, 1995.

Lyons, L. R., O. de la Beaujardière, G. Rostoker, and E. Friis-Christensen, Analysis of substorm expansion and surge development, *J. Geophys. Res., 95,* 10,575, 1990.

McPherron, R. L., C. T. Russell, and M. P. Aubry, Satellite studies of magnetospheric substorms on August 15, 1968, *J. Geophys. Res., 78,* 3131, 1973.

Opgenoorth, H. J., R. J. Pellinen, W. Baumjohann, E. Nielsen, G. Marklund, and L. Eliasson, Three-dimensional

current flow and particle precipitation in a westward traveling surge (observed during the Barium-GEOS rocket experiment), *J. Geophys. Res., 88,* 3138, 1983.

Perreault, P., and S. -I. Akasofu, A study of geomagnetic storms, *Geophys. J. R. Astron. Soc., 54,* 547, 1978.

Rich, F. J., M. S. Gussenhoven, and M. E. Greenspan, Using simultaneous particle and field observations on a low altitude satellite to estimate Joule heat energy flow into the high latitude ionosphere, *Ann. Geophys., 5A,* 527, 1987.

Richmond, A. D., Assimilative mapping of ionospheric electrodynamics, *Adv. Space Res., 12,* 59, 1992.

Richmond, A. D., Ionospheric electrodynamics using magnetic apex coordinates, *J. Geomagn. Geoelectr., 47,* 191, 1995.

Richmond, A. D., and Y. Kamide, Mapping electrodynamic features of the high-latitude ionosphere from localized observations: Technique, *J. Geophys. Res., 93,* 5741, 1988.

Richmond, A. D., et al., Mapping electrodynamic features of the high-latitude ionosphere from localized observations: Combined incoherent scatter radar and magnetometer measurements for January 18-19, 1984, *J. Geophys. Res., 93,* 5760, 1988.

Richmond, A. D., et al., Global measures of ionospheric electrodynamic activity inferred from combined incoherent-scatter radar and ground magnetometer observations, *J. Geophys. Res, 95,* 1061, 1990.

Roble, R. G., E. C. Ridley, A. D. Richmond, and R. E. Dickinson, A coupled thermosphere/ionosphere general circulation model, *Geophys. Res. Lett., 15,* 1325, 1988.

Robinson, R. M., R. R. Vondrak, K. Miller, T. Dabbs, and D. Hardy, On calculating ionospheric conductances from the flux and energy of precipitating electrons, *J. Geophys. Res., 92,* 2565, 1987.

Shue, J.-H., and D. R. Weimer, The relationship between ionospheric convection and magnetic activity, *J. Geophys. Res., 99,* 401, 1994.

Sibeck, D. G., R. E. Lopez, and E. C. Roelof, Solar wind control of the magnetosphere shape, location, and motion, *J. Geophys. Res., 96,* 5489, 1991.

Szuszczewicz, E. P., et al., *F* region climatology during the SUNDIAL/ATLAS 1 campaign of March 1992: Model-measurement comparisons and cause-effect relationships, *J. Geophys. Res.*, this issue.

Thayer, J. P., and J. F. Vickrey, On the contribution of the thermospheric neutral wind to high-latitude energetics, *Geophys. Res. Lett., 19,* 265, 1992.

Tsurutani, B. T., and W. D. Gonzalez, The efficiency of "viscous interaction" between the solar wind and the magnetosphere during intense northward IMF events, *Geophys. Res. Lett., 22,* 663, 1995.

VanZandt, T. E., W. L. Clark, and J. M. Warnock, Magnetic apex coordinates: A magnetic coordinate system for the ionospheric F_2 layer, *J. Geophys. Res., 77,* 2406, 1972.

Vickrey, J. F., R. R. Vondrak, and S. J. Matthews, Energy deposition by precipitating particles and Joule dissipation in the auroral ionosphere, *J. Geophys. Res., 87,* 5184, 1982.

Weiss, L. A., P.H. Reiff, J. J. Moses, and B. D. Moore, Energy dissipation in substorms, *Eur. Space Agency Spec. Publ. ESA-SP-335,* 309, 1992.

Winningham, J. D., et al., The UARS particle environment monitor, *J. Geophys. Res., 98,* 10,649, 1993.

Zwickl, R. D., L. F. Bargatze, D. N. Baker, C. R. Clauer, and R. L. McPherron, An evaluation of the total magnetospheric energy output parameter, UT, in *Magnetotail Physics,* pp. 155, edited by A. T. Y. Lui, Johns Hopkins Univ. Press, Baltimore, Md., 1987.

D. L. Chenette, Lockheed Palo Alto Research Laboratory, Palo Alto, CA. (e-mail: chenette@space.lockheed.com)

O. de la Beaujardière, National Science Foundation, GEO/ATM, Suite 7754, 201 Wilson Boulevard, Arlington, VA 22230. (e-mail: odelab@nsf.gov)

W. F. Denig, Phillips Laboratory, Hanscom Air Force Base, 29 Randolph Road, MA 01731-5000. (e-mail: afgl::denig)

B. A. Emery and G. Lu, High Altitude Observatory, National Center for Atmospheric Research, P.O. Box 3000, Boulder, CO 80307-3000. (e-mail: emery@hao.ucar.edu; ganglu@hao.ucar.edu)

D. S. Evans, Space Environment Laboratory, National Oceanic and Atmospheric Administration, 325 Broadway, Boulder, CO 80303. (e-mail: devans@sel.bldrdoc.gov)

R. A. Frahm and J. D. Winningham, Southwest Research Institute, 6220 Culebra Road POD 28510, San Antonio, TX 78228-0510. (e-mail: swri::rudyf; david@dewsl.space.swri.edu)

M. Lester and J. R. Taylor, Department of Physics and Astronomy, University of Leicester, University Road, Leicester LE1 7RH, England. (e-mail: nle@uk.uc.leic.ion; jrt2@ion.le.ac.ak)

A. S. Rodger, British Antarctic Survey, High Cross, Madingley Road, Cambridge CB3 OET, England. (e-mail: astro@pcmail.nerc-bas.ac.uk)

J. M. Ruohoniemi, Applied Physics Laboratory, Johns Hopkins University, Johns Hopkins Road, Laurel, MD 20723-6099. (e-mail: mike_ruohoniemi@jhuapl.edu)

(Received September 5, 1995; revised February 7, 1996; accepted February 7, 1996.)